Precambrian Research 358 (2021) 106141

Contents lists available at ScienceDirect

Precambrian Research

journal homepage: www.elsevier.com/locate/precamres

Long-lived intracontinental deformation associated with high geothermal gradients in the Seridó Belt (Borborema Province, Brazil)

Caue R. Cioffi [a,*], Vinícius T. Meira [b], Ricardo I.F. Trindade [a], Pierre Lanari [c], Carlos E. Ganade [d], Axel Gerdes [e,f]

[a] Instituto de Astronomia, Geofísica e Ciências Atmosféricas, Universidade de São Paulo, Rua do Matão, 1226, CEP 05508-090, São Paulo, SP, Brazil
[b] Departamento de Geologia e Recursos Naturais, Universidade Estadual de Campinas, CEP 13083-855, Campinas, SP, Brazil
[c] Institute of Geological Sciences, University of Bern, Baltzestrasse 1 + 3, 3012 Bern, Switzerland
[d] Serviço Geológico do Brasil – CPRM, Rio de Janeiro, Brazil
[e] Department of Geosciences, Goethe University Frankfurt, 60438 Frankfurt am Main, Germany
[f] Frankfurt Isotope and Element Research Center (FIERCE), Goethe-Universität Frankfurt, Frankfurt am Main, Germany

ARTICLE INFO

Keywords:
Intracontinental orogeny
West Gondwana
Monazite petrochronology
Low-pressure metamorphism
Quantitative compositional mapping
Iterative thermodynamic modeling

ABSTRACT

The Borborema Province (NE-Brazil) experienced widespread intracontinental deformation associated with low-pressure metamorphism during the Neoproterozoic-Cambrian assembly of West Gondwana. The widespread intracontinental deformation was driven by tectonic stresses derived from two continental collisions reported in the literature at ca. 630–610 Ma and includes the development of the continental-scale Borborema Shear Zone System. In this study, we investigate metasedimentary rocks from the Seridó Belt and eastern Patos Shear Zone, which occur in an intracontinental deformation zone at several hundred kilometers from the recognized collision zones. Using field data, quantitative compositional mapping, thermodynamic modeling, and monazite petrochronology, we constrained the metamorphic conditions and duration of intracontinental deformation in the inner Borborema Province. Monazite from leucosome-rich migmatite portions in the eastern Patos Shear Zone display $^{206}Pb/^{238}U$ dates spreading from 580 ± 13 to 512 ± 11 Ma (n = 125) with a cluster around ca. 570–550 Ma (n = 70). Staurolite-bearing schists from the western Seridó Belt display a large spread of $^{206}Pb/^{238}U$ dates between 626 ± 13 and 519 ± 12 Ma (n = 50), with a well-defined cluster between ca. 570 and 550 Ma (n = 37). Garnet-andalusite-cordierite schists from the inner and eastern Seridó Belt display monazite $^{206}Pb/^{238}U$ dates ranging from ca. 550 to 500 Ma (n = 126). Schists from the NNE-SSW striking Picuí Shear Zone in the eastern Seridó Belt exhibit Crd + And-rich nodules wrapped by the foliation, attesting the persistence of deformation after their generation. Monazite inclusions in cordierite and andalusite have REE patterns similar to matrix monazite and together they yield weighted average ages between ca. 530–525 Ma, interpreted as the age of metamorphism within the Picuí Shear Zone. Iterative thermodynamic modeling using the local bulk composition of a Crd + And-rich nodule yielded optimal *P-T* conditions of ca. 590 °C and 3.8 kbar. The presented data indicate that intracontinental deformation in the inner Borborema Province was long-lived and lasted until at least 530–525 Ma. The deformation was associated with high geothermal gradient conditions that reduced lithospheric strength allowing the development and maintenance of the Borborema Shear Zone System.

1. Introduction

Large parts of continental interiors can become reworked by widespread deformation due to plate boundary stress propagation derived from collisional processes (e.g. Avouac and Tapponnier, 1993; Raimondo et al., 2014). Intracontinental deformation is largely studied in the modern central Asia mountain ranges, including Tien Shan and Gobi-Altai orogens (Cunningham, 2005, 2013; Raimondo et al., 2014). These orogens were formed during the late Cenozoic as a distant response to the Indo-Eurasia collision and Himalayan orogeny which occurred over 2500 km to the south (e.g. Cunningham, 2013). The process of reworking large areas of former cratonic continental lithosphere in response to collisional processes is known as metacratonization (Abdelsalam et al., 2002; Liégeois et al., 2013). The extension of the

* Corresponding author.
E-mail address: caue.cioffi@yahoo.com.br (C.R. Cioffi).

https://doi.org/10.1016/j.precamres.2021.106141
Received 18 June 2020; Received in revised form 17 February 2021; Accepted 18 February 2021
Available online 25 March 2021

reworking area is controlled by the rheology of the lithosphere, which depends on its composition and thermal structure (Burov and Watts, 2006; Burov, 2011).

Intracontinental orogeny can be defined as major continental zones of crustal thickening produced at large distances from active plate margins (e.g. Raimondo et al., 2014). Transmission of plate-boundary stresses and intraplate stresses, such as vertical mantle forces, may control the evolution of orogeny at continental interiors (Aitken et al., 2013; Raimondo et al., 2014). In central Asia, the relationship between collisional forces and intracontinental deformation is self-evident (e.g. Molnar and Tapponnier, 1975; Cunningham, 2013), even though continental topographic forces might contribute to trigger and/or accelerate intraplate orogenesis (e.g. Aitken, 2011; Raimondo et al., 2014). However, the causal connection of plate-boundary processes with intraplate orogenesis is not always straightforward (e.g. Petermann and Alice Spring orogenies, Raimondo et al., 2010, 2014, and references therein). Therefore, the discussion of driving mechanisms of intracontinental orogeny is still open to debate (Raimondo et al., 2010; Aitken et al., 2013; Gorczyk et al., 2013; Gorczyk and Vogt, 2015). Based on fully coupled petrological-thermomechanical modeling, Gorczyk and Vogt (2015) showed distinct possible tectonic responses during intraplate orogeny, including mechanical removal of part of the lithosphere, intracontinental subduction, and long-term wedging of the Moho. These different tectonic responses influence localization of deformation, melt generation, ascent, and emplacement (Gorczyk and Vogt, 2015). Considering the complexity of tectonic responses associated with intraplate orogeny, one may expect a variety of evolutionary histories for different intracontinental orogens.

The Borborema Province (Fig. 1a, b), northeastern Brazil, represents a natural laboratory to study intracontinental deformation and cratonic reworking. Most of the basement in the Borborema Province is composed of Archean/Paleoproterozoic domains that were reworked during the continental collisions related to the Neoproterozoic/Cambrian amalgamation of the West Gondwana (e.g. Almeida et al., 1981; Brito Neves et al., 2000; Ganade de Araujo et al., 2014a; Neves, 2015). In the case of the Borborema Province, two quasi-orthogonal collisional orogenic events (in the western Ceará Belt and the Sergipano Orogen) (Fig. 1b), active during the late Neoproterozoic-early Cambrian (e.g. Ganade et al., 2016; Ganade de Araujo et al., 2014a,b), support the link between plate-boundary stress propagation and the widespread reworking of its inner portion. There are conflicting models in the literature regarding the pre-Brasiliano (i.e. before 650 Ma) evolution of the Province, with some arguing in favor of an accretionary evolution with orogenic processes and terrane accretion at the early Neoproterozoic (Tonian) (e.g. Padilha et al., 2016; Santos et al., 2018) and others arguing that the Province was already amalgamated and stable since the Paleoproterozoic (Neves, 2003, 2015). In both mentioned scenarios, the whole province would be a coherent continental block since at least the early Neoproterozoic.

The widespread reworking of the Borborema Province continental block associated with the West Gondwana assembly led to the generation of one of the largest shear zone systems in the world which includes the Borborema Shear Zone System (Vauchez et al., 1995) and its counterpart in Africa (the Trans-Saharan Orogen) (Caxito et al., 2020, and references therein). The major strike-slip shear zones of the Borborema Shear Zone System (i.e. Patos and Pernambuco) are more than 600 km long and up to 30 km wide, displaying general E-W trend and dextral movement. These major shear zones are connected to minor NE-SW

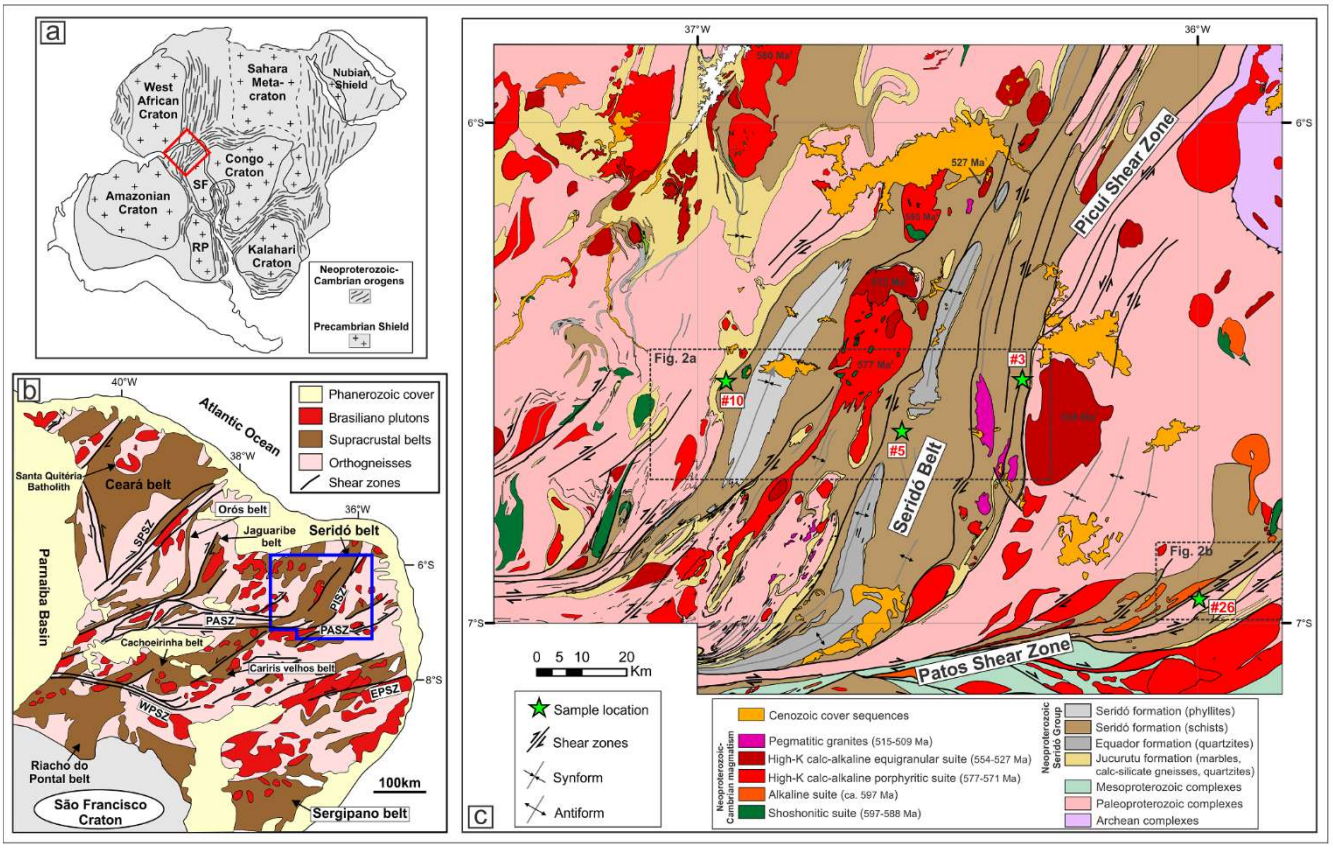

Fig. 1. (a) Schematic reconstruction of western Gondwana with location of Borborema Province (modified from Gray et al., 2008); (b) Sketch tectonic map of the Borborema Province with location of Fig. 1c (modified from Neves, 2003, 2015). Main shear zones: WPSZ, West Pernambuco; EPSZ, East Pernambuco; PASZ, Patos; SPSZ, Senador Pompeu; PISZ, Picuí; (c) Geological map of the Seridó Belt with location of the analyzed samples (modified from Guimarães et al., 2007; Rodrigues and Medeiros, 2015; Cavalcante et al., 2016). References of magmatic ages: 1 – Hollanda et al. (2017); 2 – Archanjo et al. (2013); 3 – Long et al. (2019). Outcrop locations: #3(S 6°30′30.68″/W 36°20′57.18″); #5(S 6°36′53.85″/W 36°35′29.53″); #10(S 6°30′54.77″/W 36°56′35.64″); #26(S 6°57′2.70″/W 35°59′49.32″).

striking strike-slip shear zones (~100–200 km long) forming a coherent system that extends over more than 200.000 km^2 (Vauchez et al., 1995), crosscutting Archean/Paleoproterozoic basement rocks and Neoproterozoic metasedimentary sequences (Fig. 1b). These shear-zones exerted important structural control on the emplacement of the Neoproterozoic granitoids and on the mineral deposits, especially on the Be-Ta-Li-bearing pegmatites and shear-related gold deposits in the Seridó Belt (Fig. 1c; Araújo et al., 2001, 2005).

Even considering the conflicting evolutionary models for the Borborema Province mentioned above, the Borborema Shear Zone System (Vauchez et al., 1995) might be treated as the result of intracontinental reworking of Archean/Paleoproterozoic basement rocks driven by convergent plate-boundary stresses. Old cratonic domains are characterized by the presence of thick (>250 km) and cold lithospheric roots making them stiff and hard to deform (e.g. Jordan, 1975; Michaut et al., 2009). Therefore, the study of old cratonic domains reworked during later orogenic processes, like the Borborema Province, can provide valuable information about the mechanisms of lithospheric roots removal and metacratonization and how these processes can shape Earth's continents. In this regard, it is important to mention the recent controversies on the processes that assembled the Gondwana continent (e.g. Konopásek et al., 2020). Recent proposed tectonic models reinterpreted some orogenic belts formerly considered plate boundary orogens as intracontinental orogenies (e.g. the Ribeira Belt and the Araçuaí Orogen) (Meira et al., 2015, 2019; Fossen et al., 2020), emphasizing the importance of intracontinental deformation in shaping the West Gondwana.

A common feature of metacratonized areas around the world is the occurrence of low-pressure (high *T/P*, i.e. high geothermal gradients) metamorphic assemblages associated with widespread post-collisional magmatism (e.g. Liégeois et al., 2013). Indeed, high geothermal gradients play a key role on softening the continental lithosphere, allowing extensive intracontinental reworking (e.g. Cunningham, 2013; Raimondo et al., 2014). In this contribution, we present a detailed study of low-pressure metasedimentary rocks located far (~500 km in present day coordinates) from the Borborema Province recognized collisional fronts (the western Ceará Belt and the Sergipano Orogen), within the Seridó Belt and the eastern Patos Shear Zone. The goal of this study is to better understand the intracontinental deformation and metamorphism in the inner Borborema Province. The age and *P-T* conditions of the low-pressure metamorphism and intracontinental deformation were constrained based on a combination of field data, petrography, quantitative compositional mapping, thermodynamic modeling, and monazite petrochronology. This is the first study to determine in-situ isotopic monazite ages (LA-ICP-MS) for the inner Borborema Province low-pressure metamorphic rocks. The new data bring important insights on the age and duration of the low-pressure metamorphism and its role in the generation and maintenance of the Borborema Shear Zone System, which is among the largest strike-slip shear zone systems on Earth. The results are also used to discuss key reworking processes of old cratonic domains and intraplate tectonics.

2. Geological setting

2.1. Borborema Province

The Borborema Province, located in northeastern Brazil, experienced widespread deformation and metamorphism associated with long-lasting magmatism during the Neoproterozoic-Cambrian assembly of the West Gondwana (e.g. Almeida et al., 1981; Brito-Neves et al., 2000; Ganade de Araujo et al., 2014a, 2014b). At that time, the province was among the Amazonian, West Africa and São Francisco-Congo cratons (Fig. 1a) and, as a result of the collision of these cratons, one of the Earth's largest strike-slip shear zone systems, the so called Borborema Shear Zone System (Vauchez et al., 1995), was generated. The basement of the province comprises mainly Paleoproterozoic orthogneisses (e.g. Hollanda et al., 2011; Santos et al., 2015; Souza et al., 2016; Jardim de Sá et al., 1995) and minor Archean domains (Dantas et al., 2004, 2013; Ganade et al., 2017). Tonian volcano-sedimentary sequences and orthogneisses with ages ranging from ca. 995 to 950 Ma (Cariris Velhos event; Fig. 1b) (Van Schmus et al., 1995, 2011; Santos et al., 2010) display intraplate geochemical signatures (Guimarães et al., 2012) and occur mainly in the central part of the province marking an important period of continental extension (Neves, 2003). The basement rocks are partially covered by metasedimentary successions mainly deposited during the late Neoproterozoic in a continental setting (e.g. Van Schmus et al., 2003; Neves, 2015) (Fig. 1b). Extensive magmatism between ca. 650 and 500 Ma is recorded by a large number of batholiths and smaller plutons along the province, including arc-related, *syn*-collisional and post-collisional magmatism (e.g. Ganade de Araujo et al., 2014a; Neves, 2015) (Fig. 1b).

The Neoproterozoic-Cambrian evolution of the Borborema Province consists of two continental collisions (Ganade de Araujo et al., 2014a, 2014b). One between the West African Craton and the Benino-Nigerian shield, that was physically continuous with the northern Borborema Province, occurred at ca. 620–610 Ma, with a late lateral juxtaposition of the northwestern Borborema Province and the Parnaíba block due to dextral shearing along the Transbrasiliano-Kandi shear zone (Ganade et al., 2016; Ganade de Araujo et al., 2014a). This collisional event is recorded by ultra-high pressure (UHP) eclogitic rocks in the Ceará domain with peak metamorphism dated in zircon rims at ca. 615 Ma (Santos et al., 2009, 2015; Ganade de Araujo et al., 2014b) and by pre-collisional arc magmatism in the Santa Quitéria batholith, between 650 and 620 Ma (Fetter et al., 2003; Ganade de Araujo et al., 2012). The other event relates to the collision between the São Francisco Craton and the southern Borborema Province associated with the development of the Sergipano Orogen which displays *syn*-collisional granitoids dated at ca. 630–610 Ma (Bueno et al., 2009; Oliveira et al., 2010; Pereira et al., 2020). In the context of these two continental collisions, the extensive intracontinental deformation observed within the province (Neves, 2015; Neves et al., 2017) and including the generation of the continental-scale Borborema Shear Zone System (Vauchez et al., 1995) (Fig. 1b) can be linked to propagation of tectonic stresses from one or both collisional systems.

Two large (>600 km long and up to 30 km in width) ~E-W striking strike-slip shear zones, crosscutting basement and metasedimentary rocks, occur in the inner portion of the province (i.e. the Patos and Pernambuco shear zones) (Fig. 1b). These major shear zones are connected with minor (~100–200 km long) NE-SW/NNE-SSW striking strike-slip and oblique shear zones (e.g. the Picuí Shear Zone) (Fig. 1b, c) (e.g. Vauchez et al., 1995; Neves et al., 2000). The metasedimentary sequences, including the Seridó, Cachoeirinha and Jaguaribe belts, are generally oriented parallel to these minor NE-SW striking shear zones (Fig. 1b). Deformation in this inner part of the Borborema Province is frequently associated with low-pressure (~3–6 kbar) and medium- to high-temperature (~500–700 °C) metamorphism (Lima, 1992; Vauchez et al., 1995; Neves et al., 2000; Archanjo et al., 2013). The main shear zones (i.e. Patos and Pernambuco) display high-temperature (~700 °C) mylonites with evidence of partial melting (Vauchez and Egydio-Silva, 1992; Viegas et al., 2013, 2014).

Zircon rims from mylonitic migmatites within the Patos Shear Zone yield U-Pb ages ranging between ca. 573 and 562 Ma (Ion microprobe dating; 1–2% uncertainties) (Archanjo et al., 2013; Viegas et al., 2014), which have been interpreted as the age of high-temperature metamorphism within the shear zone. Slow cooling rates after peak conditions are suggested by ^{40}Ar-^{39}Ar thermochronology, including amphibole plateau ages (mainly between 545 and 535 Ma) and muscovite plateau ages (ca. 520–500 Ma) (Corsini et al., 1998; Araújo et al., 2005). Biotite grains show higher data spread with ages ranging from ca. 560 to 500 Ma (Corsini et al., 1998). This high age spread is most likely related to excess argon (Corsini et al., 1998) and the biotite ages older than ca. 505 Ma are considered as not reliable. All available

metamorphic U-Pb ages of zircon are from high-temperature (~700 °C) samples that occur within the main shear zones. No data from the medium-temperature (~500–600 °C) samples that occur within the metasedimentary belts (i.e. Jaguaribe and Seridó belts) (Fig. 1b) are available in the literature so far.

2.2. Seridó Belt

The Seridó Belt is an approximately 200 km long and 30–70 km wide NE-SW striking metasedimentary belt located in the northeastern Borborema Province. The belt is limited to the south by the dextral E-W striking Patos Shear Zone and its north portion is covered by Mesozoic sediments of the Potiguar Basin (Fig. 1b, c) (e.g. Jardim de Sá et al., 1995; Caby et al., 1995; Araújo et al., 2001; Van Schmus et al., 2003; Archanjo et al., 2013; Hollanda et al., 2015). The Seridó Belt eastern boundary is defined by the NNE-SSW to NE-SW striking Picuí Shear Zone that displays inverse movement with lateral component (Fig. 1c and Fig. 2a). The main deformation phase in the Seridó Belt is characterized

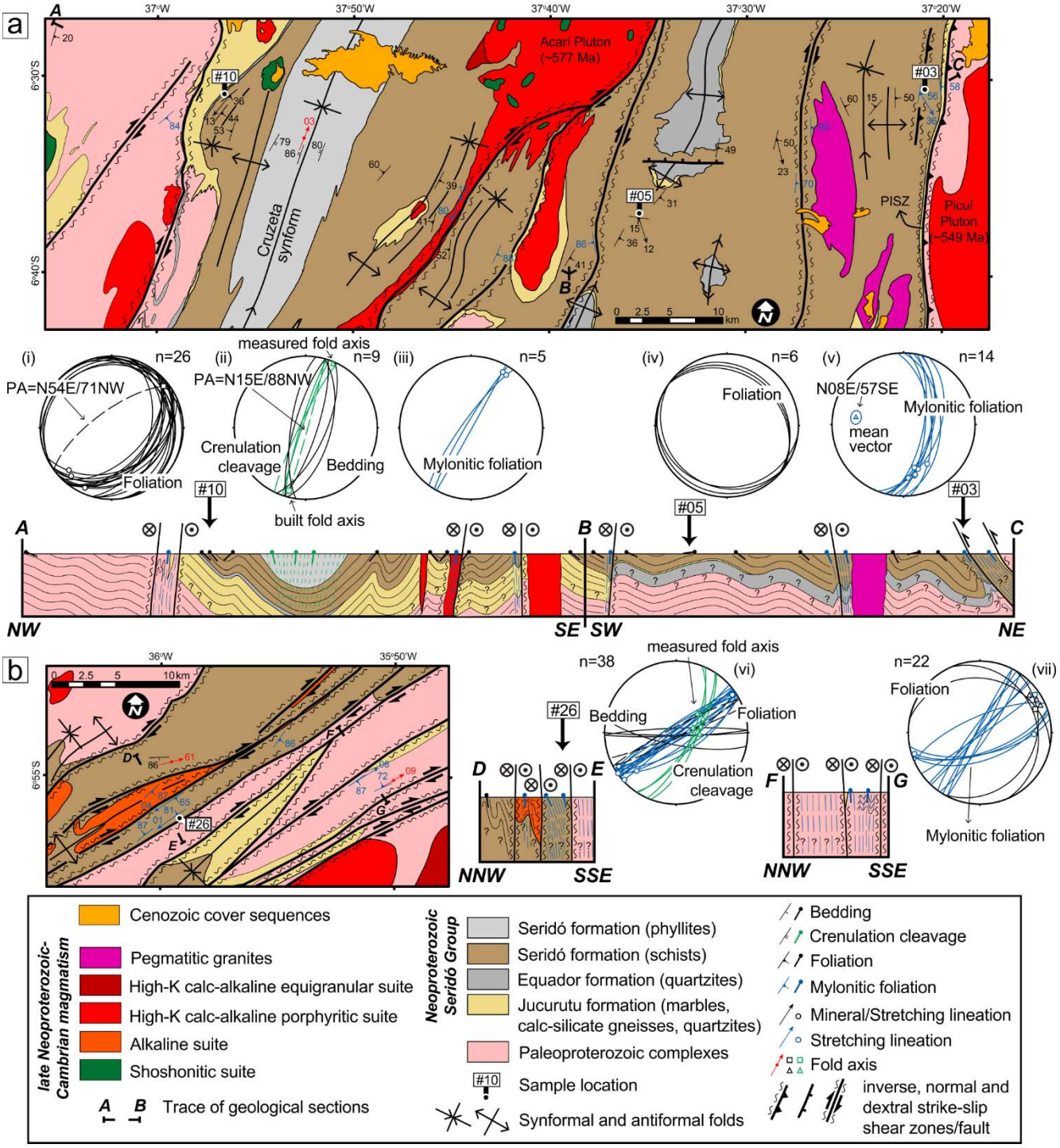

Fig. 2. Geological maps and cross sections along the central Seridó Belt (a) and part of the eastern Patos Shear Zone (b), based on available 1:100,000 and 1:250,000 scale geological maps (Bezerra et al., 2009; Cavalcante et al., 2016; Cavalcante et al., 2018; Guimarães et al., 2007) and our own observations. Lower hemisphere equal area stereograms (i-vii) are also shown above the cross sections. Abbreviation, PISZ: Picuí Shear Zone.

by a dextral transpressive regime (Archanjo et al., 2002) that generated upright to inclined folds with general sub-horizontal NE-SW striking axis and associated shear zones (Fig. 1c). This deformation phase overprints a shallow dipping foliation attributed by some authors to a previous thrusting regime (e.g. Araújo et al., 2003; Archanjo et al., 2013). Basement rocks consist mainly of Paleoproterozoic (ca. 2.25–2.15 Ga) high-K calc-alkaline orthogneisses related to the Caicó Complex (Jardim de Sá et al., 1995; Souza et al., 2007). Archean rocks of the São José do Campestre massif (ca. 3.45–2.70 Ga) (Dantas et al., 2004, 2013) occur within Paleoproterozoic orthogneisses near the northeast boundary of the Seridó Belt (Fig. 1c).

The metasedimentary sequence comprises from bottom to top: (1) the lower Jucurutu Formation which consists of impure carbonates, calc-silicate gneisses, paragneisses, impure quartzites and amphibolites; (2) the middle Equador Formation including quartzites and conglomeratic layers and (3) the upper Seridó Formation constituted by metapelites ranging from phyllites to mica schists (e.g. Jardim de Sá, 1994; Caby et al., 1995; Van Schmus et al., 2003). It is important to mention that there is still a debate about the Seridó Belt stratigraphy and recently, Hollanda et al. (2015) have placed the Equador Formation at the base of the stratigraphic sequence. Detrital zircon provenance studies indicate late Neoproterozoic (ca. 650–610 Ma) maximum depositional ages for the Jucurutu and Seridó formations (Van Schmus et al., 2003; Hollanda et al., 2015), which were most likely deposited in a continental setting. The Seridó Formation phyllites (Fig. 3a) were metamorphosed at greenschist facies and occur within synformal structures at the top of the metasedimentary sequence (Fig. 1c, 2a). The mica schists (Fig. 3b, c and 4) have Grt + Bt + Pl + Qz ± Ms ± St ± Crd ± And ± Sil ± Ilm (mineral abbreviations after Whitney and Evans, 2010) as rock-forming minerals. Low pressure amphibolite facies metamorphic conditions of ca. 500–600 °C, 2.5–4 kbar and an eastward increase in metamorphic grade were recognized by Lima (1992) based on conventional thermobarometry.

Several Neoproterozoic-Cambrian igneous bodies intruded the metasedimentary sequences and basement orthogneisses (Fig. 1c and 2a). Based on geochemical signatures, the plutonic rocks occurring in the studied area can be divided into five main igneous suites (Nascimento et al., 2015 and reference therein) (Fig. 1c): (1) the shoshonitic suite which is composed of K-rich gabbros and diorites (U-Pb zircon ages between 597 ± 6 and 588 ± 6 Ma); (2) the alkaline suite including syenogranites and syenites (age not well constrained, only one U-Pb zircon age at 597 ± 4 Ma; Souza et al., 2016); (3) the high-K calc-alkaline porphyritic suite comprised by monzonites and granodiorites with K-feldspar phenocrysts up to ~15 cm long (U-Pb zircon ages between 577 ± 5 and 571 ± 3 Ma); (4) the high-K calc-alkaline equigranular suite including fine- to medium-grained monzogranites (U-Pb zircon ages between 554 ± 10 and 527 ± 8 Ma) and (5) the pegmatitic granites (U-Pb columbite-tantalite ages between 515 ± 1 and 509 ± 3 Ma; Baumgartner et al., 2006).

3. Structural geology

Three geological cross sections across the central Seridó Belt and eastern Patos Shear Zone (Fig. 2) were described in order to better understand the relationship between structural fabrics and metamorphic assemblages. The main planar fabric (Sn) in the central Seridó Belt is defined by sedimentary bedding in folded phyllites (Fig. 2a and 3a), pervasive schistosity in mica schists (Fig. 2a and 3b, c) and gneissic banding in paragneisses and orthogneisses. Rootless intrafolial folds are commonly observed within folded gently dipping Sn schistosity, including in the western and inner portion of the central Seridó Belt (Fig. 2a and 3c). The main Sn planar fabric is deformed by NE-SW/NNE-SSW striking upright to gently inclined subhorizontal folds (Fig. 2i, ii), varying from open to tight folds towards the transposing shear zones (Fig. 2a). Minor NW-SE striking gentle to open upright subhorizontal folds also occur (Fig. 2iv). Strain localization along hinge zones developed a transpositional Sn + 1 planar fabric defined by crenulation cleavage in phyllites (Fig. 2a, ii and Fig. 3a). Strain localization within

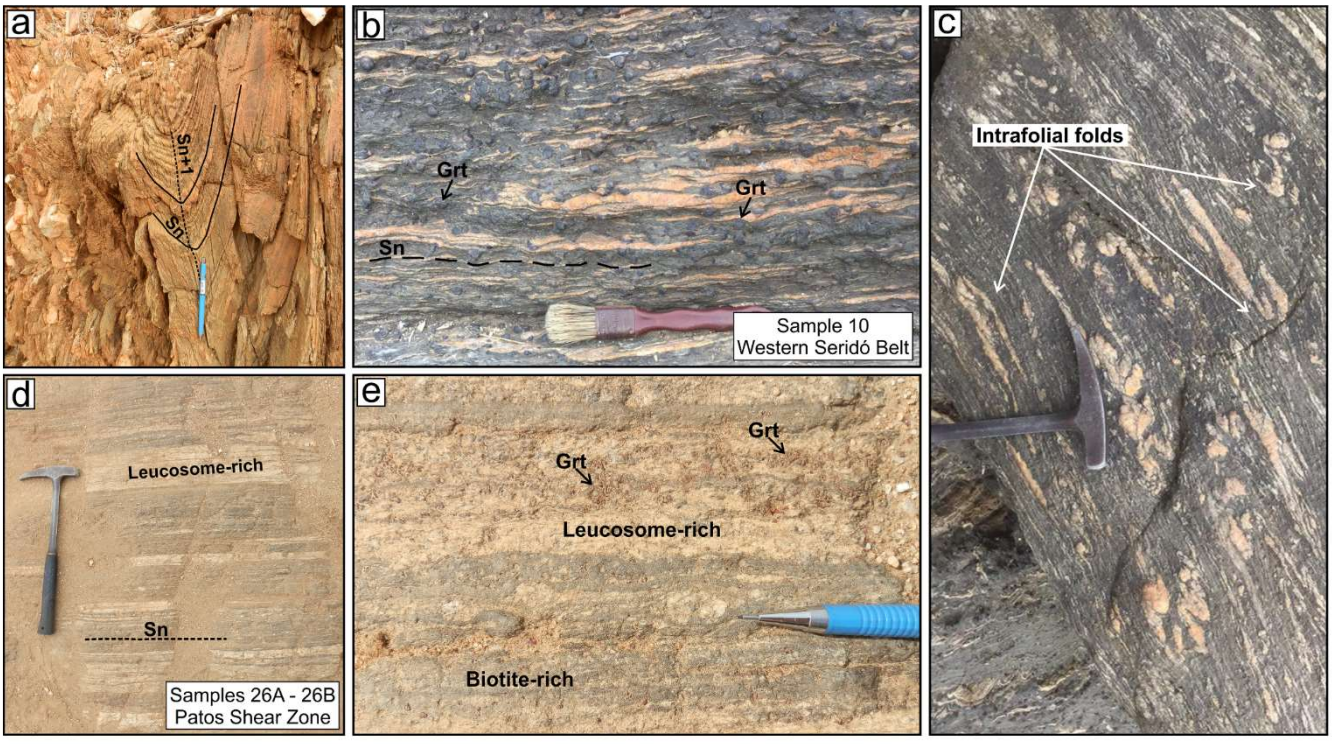

Fig. 3. Field aspects of the Seridó Belt and eastern Patos Shear Zone rocks. (a) Folded phyllites occuring at the top of the metasedimentary sequence within the Cruzeta synformal structure in the western Seridó Belt (Sn + 1 = N20E/80NW, Fig. 2a, ii); (b) Porphyroblastic garnet-staurolite schist from the western Seridó Belt with garnet porphyroblasts up to 2 cm in diameter (Sn: N50E/30SE, Fig. 2a, i); (c) Intrafolial folds within garnet-staurolite schist from the western Seridó Belt; (d, e) Garnet-bearing mylonitized metatexites from the eastern Patos Shear Zone (Sn: N60E/80SE, Fig. 2b, vi).

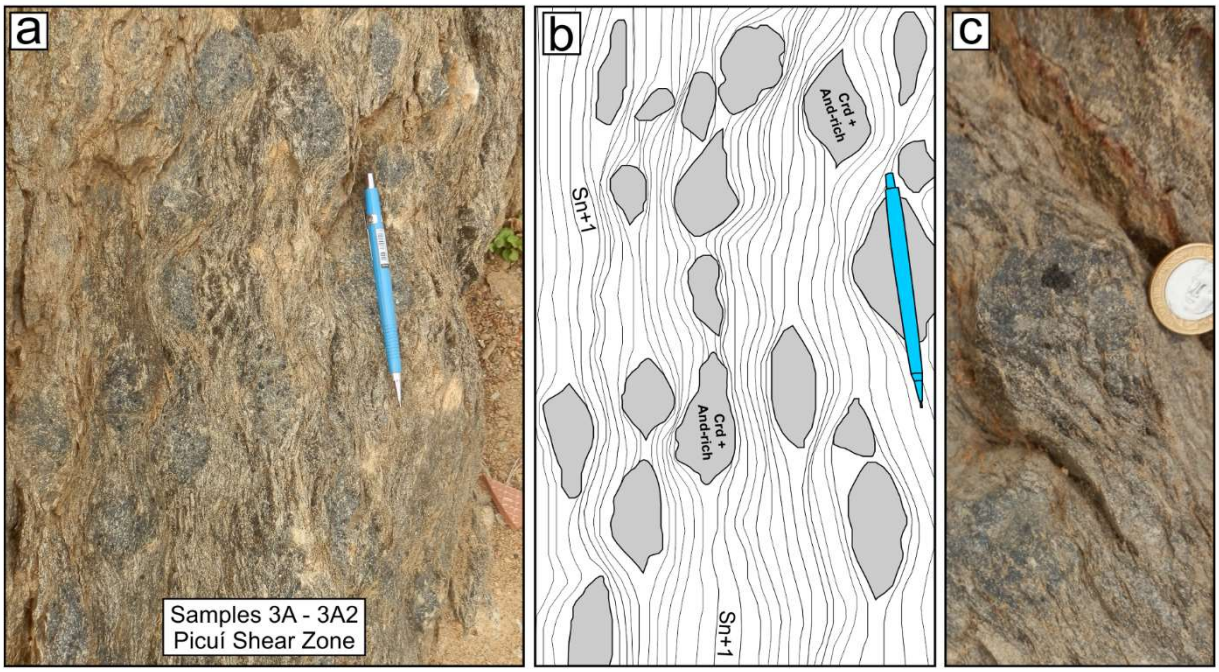

Fig. 4. Field aspects of the cordierite + andalusite-bearing schists within the Picuí Shear Zone, eastern Seridó Belt (samples 3A - 3A2). (a) Eye-shaped cordierite + andalusite-rich nodules, up to 10 cm in length, elongated parallel to the shear zone main foliation (Sn+1: N15E/65SE); (b) Sketch of Fig. 4a; (c) Close-up of a cordierite + andalusite-rich nodule displaying the foliation wrapping around the nodules.

shear zones developed mylonitic foliation in gneisses and schists (Fig. 2a, iii, v, Fig. 3d, e and Fig. 4). The mylonitic fabric has steep dip and strike varying from NNE-SSW to NE-SW (Fig. 2a, ii, iii). Most NNE-SSW striking shear zones in the central Seridó Belt have subhorizontal stretching lineation (Fig. 2a, iii) and are considered dextral strike-slip shear zones. The ~N-S striking (mean orientation N08E/57SE) Picuí Shear Zone has S-SSE trending moderately plunging stretching lineation (Fig. 2a, v) and is interpreted in this study as an inverse shear zone with sinistral lateral component (Fig. 2a, v). Detailed kinematic and vorticity analysis are necessary to test this hypothesis.

The geological sections described in the eastern Patos Shear Zone show a prominent and pervasive steep dipping NE-SW to ENE-WSW striking mylonitic foliation (Fig. 2b, vi, vii and Fig. 3d, e). The stretching lineation associated with the mylonitic foliation is subhorizontal (Fig. 2vi, vii) and dextral kinematics is well defined by porphyroclasts and asymmetric drag folds. Previous planar fabrics can be observed in low strain zones, usually defining close to tight subhorizontal upright folds (Fig. 2b, vii). It is important to mention that the eastern segment of the Patos shear zone has been called Remígio-Pocinhos Shear Zone by Souza et al., (2006).

4. Sample description and petrography

Samples from the eastern Patos Shear Zone and across the Seridó Belt were selected for in-situ U-Pb monazite geochronology investigation in order to constrain the timing of deformation and metamorphism along the Seridó Belt and its major shear zones. These samples include two garnet-bearing mylonitized migmatites occurring within the major ENE-WSW strike-slip Patos Shear Zone (samples 26B and 26A) (Fig. 2b; Seridó Belt southern boundary) and garnet-bearing schists that occur within the NE-SW striking Seridó Belt (Fig. 2a). Samples from the Seridó Belt include rocks with gentle to moderate dipping foliations in the western and inner portions of the central Seridó Belt (samples 10 and 5, respectively) (Fig. 2a), and samples from the NNE-SSW striking Picuí Shear Zone (samples 3A and 3A2) (Fig. 2a; Seridó Belt eastern boundary). Sample 10 is a garnet-staurolite-biotite schist, whereas sample 5 is a garnet-andalusite-sillimanite-cordierite-biotite schist. The samples from the Picuí Shear Zone (sample 3A and 3A2) consist of garnet-andalusite-cordierite-biotite schists.

4.1. Samples 26B and 26A

These samples from the eastern Patos Shear Zone are deformed stromatic garnet-biotite metatexites with stripped structure composed of alternating layers of recrystallized feldspars and quartz ribbons (Fig. 3d, e). Sample 26B is from a leucosome-rich layer of granodioritic composition. Feldspars (45–50 vol%) occur as fine-grained (0.5–1 mm) recrystallized granoblastic aggregates and also as porphyroclasts up to 3 mm in length. Plagioclase porphyroclasts (2–3 mm long) locally display antiperthitic exsolution lamellae. Quartz (35–40 vol%) is stretched and occurs as ribbons within the foliation (N60E/80SE) (Fig. 5a). Biotite (5–7 vol%) consists of fine-grained flakes (<1mm long) oriented along the foliation. Garnet grains (5–7 vol%) ranging from 0.5 to 4 mm in size are subidioblastic and poikiloblastic, rich in amoeba-shaped quartz inclusions (0.1 to 0.5 mm in size). Monazite occurs as 10 to 80 μm long inclusions in biotite grains and also as large, up to ca. 200 μm long, euhedral grains associated with the leucocratic layers (Fig. 5a). Other accessory minerals include chlorite and zircon. Sample 26A is from a biotite-rich (15–20 vol%) layer and displays banded structure with stromatic leucosomes of granodioritic composition, ranging from 0.1 to 1 cm in thickness, parallel to the main foliation. Garnet crystals (0.3 to 3 mm in diameter) occur mainly within the fine- to medium-grained biotite-rich layers. The smaller garnet grains are subidioblastic to idioblastic and usually inclusion-free, while larger grains (2–3 mm in diameter) are poikiloblastic, rich in amoeba-shaped quartz inclusions (0.1 to 0.5 mm in size) (Fig. 5b). Plagioclase displays fine- to medium-grained granoblastic texture and locally antiperthitic exsolution lamellae. Quartz occurs as ribbons within the main foliation. Monazite grains ranging from ca. 20–50 μm in size are associated with the biotite-rich layers and locally are present as inclusions in garnet. Other common accessory minerals include muscovite, chlorite, apatite and zircon.

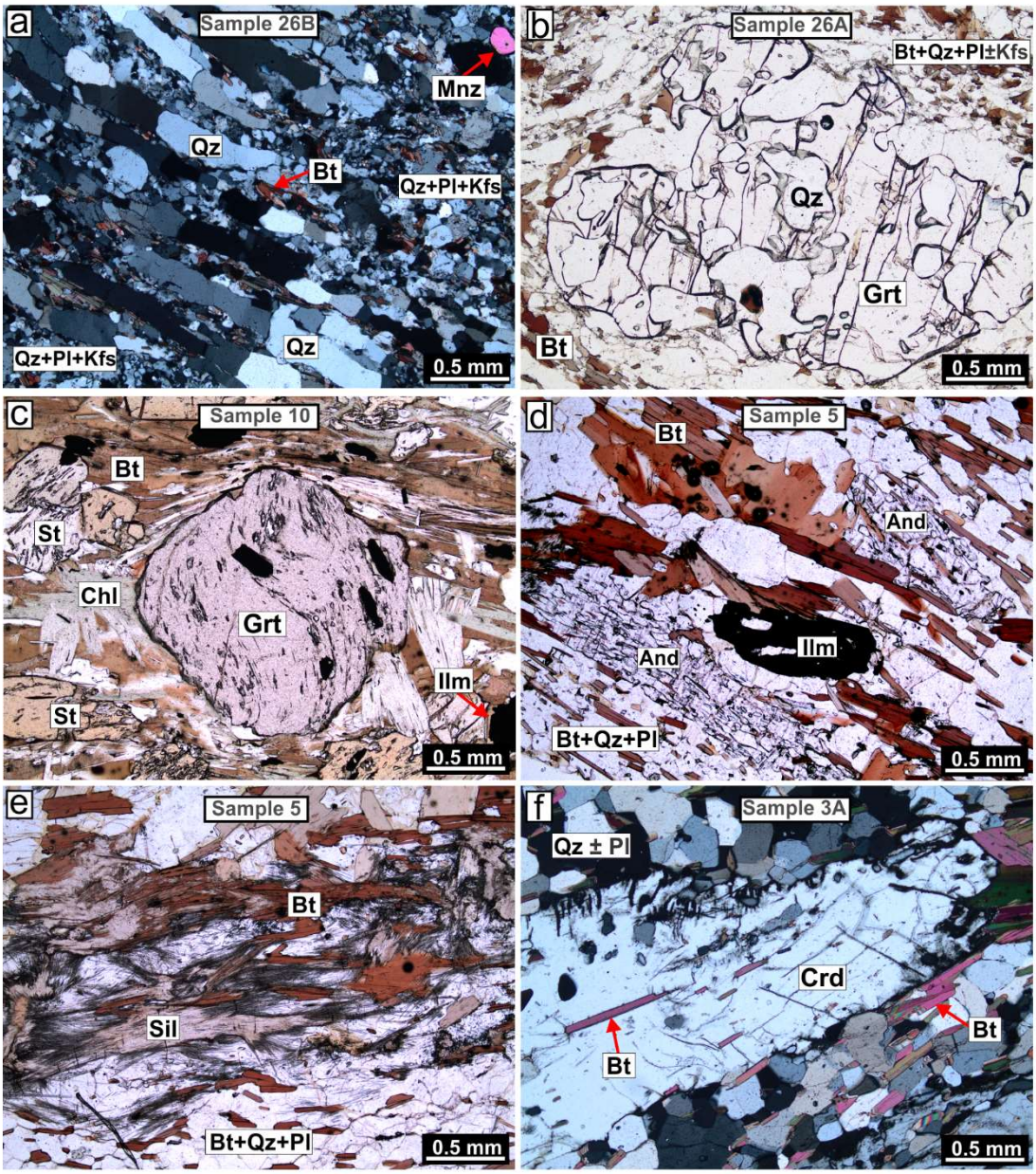

Fig. 5. Photomicrographs of the analyzed samples. (a) Deformed leucosome-rich migmatite layer displaying quartz ribbons. Note the occurrence of a large, ca. 200 μm long, monazite grain at the photo upper right (sample 26B); (b) Garnet porphyroblast in a biotite-rich migmatite layer displaying amoeba-shaped quartz inclusions (sample 26A); (c) Intertectonic garnet and staurolite grains (sample 10); (d) Elongated andalusite crystals parallel to the schist main foliation (sample 5); (e) Fibrous sillimanite partially replacing biotite along the main foliation (sample 5); (f) Elongated cordierite grain parallel to the schist main foliation. Note the parallelism between internal and external foliations indicating that the grain was not rotated after its formation (sample 3A).

4.2. Sample 10

This sample is a garnet-staurolite-biotite schist from the western Seridó Belt (Fig. 2a and Fig. 3b, c). It has foliated structure and porphyroblastic texture. Abundant (35–40 vol%) up to 2 mm long biotite flakes define the foliation (N50E/30SE) (Fig. 2a, iii and Fig. 5c). Quartz (20–25 vol%) and plagioclase (5%) occur as fine-grained recrystallized aggregates. Garnet (10–15 vol%) and staurolite (5–10%) porphyroblasts, up to 5 and 2 mm in length, respectively, display folded internal foliations defined by trails of tiny quartz and ilmenite inclusions. These syntectonic inclusion trails, within garnet and staurolite, are wrapped by a later fabric in the whole-rock, characterizing the porphyroblasts as intertectonic (Fig. 5c). The biotite crystals are partially replaced by late chlorite + white mica (Fig. 5c). Small monazite grains, ranging from ca. 10–50 μm, form inclusions in biotite and locally in staurolite.

4.3. Sample 5

This sample is a garnet-andalusite-sillimanite-cordierite-biotite schist that occurs near to the center of the Seridó Belt. It occurs in a region of flat-lying foliation (N70W/15SW) (Fig. 2a, iv) located far away from the main shear zones. It exhibits a foliated structure and fine- to medium-grained inequigranular texture. Biotite flakes (20–25 vol%) up to 1 mm long define the foliation. Most of the quartz (45–50 vol%) and plagioclase (5–10%) occur as fine-grained recrystallized aggregates, while larger quartz grains, up to 1 mm in length, are stretched within the foliation. Andalusite (3–5 vol%) and cordierite (5–7%) porphyroblasts, up to ca. 4 mm long, are elongated and oriented along the foliation (Fig. 5d). These grains are poikiloblastic, rich in biotite and quartz inclusions, which define internal foliations parallel to the matrix foliation. Garnet grains (3–5 vol%) from 0.5 up to 2 mm diameter display cores

rich in quartz inclusions and thin inclusion-free outer rims. These garnet grains were partially replaced by cordierite + biotite intergrowths. Fibrous sillimanite (3–5 vol%) partially replaced biotite along the foliation (Fig. 5e). Late decussate white mica occurs associated with biotite-rich layers. Small subidioblastic monazite inclusions (20 to 50 μm in length) developed strong pleochroic haloes in biotite (Fig. 5d). Other accessory minerals include ilmenite and apatite.

4.4. Samples 3A and 3A2

These samples are garnet-andalusite-cordierite-biotite schists from the eastern Seridó Belt, which occur within a N-S/NNE-SSW striking

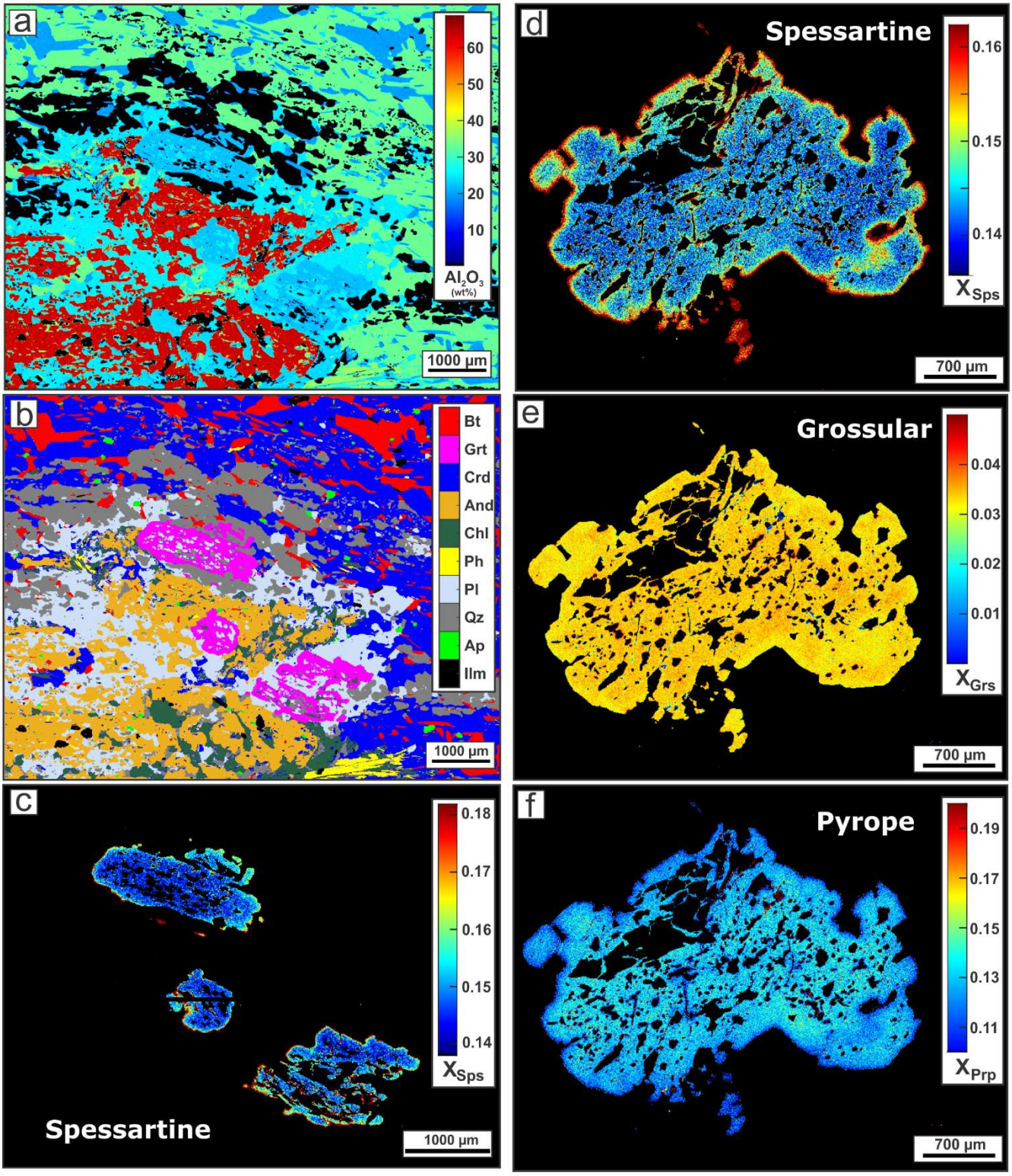

Fig. 6. (a) Quantitative Al_2O_3 (wt%) compositional map of a cordierite + andalusite-rich nodule from sample 3A2 (see Supplementary data 4 for the location of the maps); (b) Mineral phases map of the area pictured in Fig. 6a; (c) Quantitative compositional map of spessartine fraction for the garnet grains displayed in Fig. 6a. (d-f) Quantitative compositional maps of spessartine, grossular and pyrope fractions (d, e and f respectively) for a garnet porphyroblast of sample 3A2.

shear zone system, known as Picuí Shear Zone (Fig. 1b, c and Fig. 2a). The schists are characterized by the presence of lenticular eye-shaped cordierite + andalusite-rich nodules elongated along the ~NNE-SSW striking foliation (N10E/60SE) (Fig. 2a, v and Fig. 4). These nodules are up to ~8 cm in length, medium- to coarse-grained and are wrapped by the matrix foliation defined by biotite + quartz + plagioclase (Fig. 4). The nodules are constituted of cordierite (~30 vol%) + quartz (~20%) + andalusite (~15%) + plagioclase (~15%) + biotite (~10%) + garnet (~5%) + ilmenite (~1%) (Fig. 6a, b). The cordierite grains are poikiloblastic, rich in biotite inclusions. Isolated cordierite grains are elongated and display internal foliations, defined by biotite inclusions, oriented parallel to the matrix foliation (Fig. 5f). Late decussate fine-grained chlorite (~5 vol%) and muscovite (~1%) aggregates occur within cordierite + andalusite-rich domains. Garnet grains up to ~ 2–3 mm in length occur within the cordierite + andalusite-rich domains and also as isolated grains within the matrix. The garnet grains have inclusion-rich cores with internal foliations defined by plagioclase and quartz inclusions. These internal foliations are discordant with the matrix foliation and the garnet cores are wrapped by a succession of thin inclusion-free outer rims. Monazite occurs as subidioblastic to idioblastic small inclusions (20–50 μm) in matrix biotite and also as larger, up to 150 μm in size, irregular-shaped grains included in cordierite and andalusite. Other accessory minerals include apatite and tourmaline.

5. Mineral compositions and phase equilibrium modeling

Major mineral compositions and phase equilibrium modeling of the garnet-andalusite-cordierite-biotite sample 3A2 from the Picuí Shear Zone in the eastern Seridó Belt (Fig. 1c) is presented in this section. To investigate the compositional variability of the mineral phases, X-ray maps were acquired using an electron probe microanalyzer (EPMA) and converted into oxide weight percent maps by applying the internal standard technique (De Andrade et al., 2006) implemented in the software XMapTools 2.2.1 (Lanari et al., 2014, 2019). Isochemical phase diagrams in the system MnO-Na_2O-CaO-K_2O-FeO-MgO-Al_2O_3-SiO_2-H_2O-TiO_2 were produced with the software Theriak-Domino (de Capitani and Brown, 1987; de Capitani and Petrakakis, 2010) using the internally consistent thermodynamic dataset TC55 (modified from Holland and Powell, 1998). The following solid solution models were used: feldspar (Baldwin et al., 2005); garnet, biotite (White et al., 2005); cordierite, staurolite (Holland and Powell, 1998); chloritoid (White et al., 2000); chlorite (Holland et al., 1998); white mica (Coggon and Holland, 2002); ilmenite and melt (White et al., 2007).

A *P–T* isochemical phase diagram of sample 3A2 was calculated using the local bulk composition of a Crd + And-rich nodule and assuming water-saturated conditions. The bulk-composition was obtained by integrating density-corrected compositional maps using XMapTools (Lanari et al., 2014; Lanari & Engi, 2017; Fig. 6a, b). Optimal *P–T* conditions of sample 3A2 were obtained using the software solution Bingo-Antidote (Lanari & Engi, 2017; Lanari & Duesterhoeft, 2019; Duesterhoeft and Lanari, 2020) implemented in XThermoTools 1.1.2 and the same thermodynamic database TC55. These iterative thermodynamic models are based on a statistical comparison between the modelled and observed mineral assemblage, modes and compositions that quantifies how the model reproduces the observations for the investigated volume (Duesterhoeft and Lanari, 2020). The scoring part (Bingo) is based on three statistical model quality factors ranging between 0% (bad model) and 100% (perfect model): Q_{asm} for the assemblage, Q_{vol} for the mineral modes, Q_{cmp} for the mineral compositions. The inversion (Antidote) is performed on a global evaluation criterion Q_{total} and allows optimal *P–T* conditions to be obtained for the formation of minerals within the Crd + And-rich nodule. It has been demonstrated that in the case of a well-equilibrated mineral assemblage, the volume of the investigated domain and the mineral proportions do not affect the *P–T* conditions obtained by Antidote (Lanari & Hermann, 2020). Additionally, isochemical phase diagrams based on whole-rock compositions obtained by XRF were calculated for samples 5 and 10. These diagrams are presented in the Supplementary figure 1. Average mineral compositions of sample 3A2 and the bulk-compositions used for thermodynamic modeling are given in Supplementary data 1.

Garnet grains from the Grt-And-Crd-Bt schist sample 3A2 ranging from 1 to 3 mm in diameter display unzoned cores with an average composition of $Alm_{70}Prp_{12}Grs_4Sps_{14}$. These grains have a slightly increase in manganese contents (up to Sps_{17}) (Fig. 6c, d) in the outer rims (20–30 μm width) which are associated to slightly decrease in grossular and pyrope contents (Fig. 6e, f). The poikiloblastic cordierite grains do not show expressive compositional zoning with XFe (Fe^{2+}/ Fe^{2+}+ Mg) ranging between 0.35 and 0.40 with an average of ~0.37. Matrix biotite and biotite inclusions in cordierite poikiloblasts have XFe values ranging from 0.50 to 0.54 and Ti a.p.f.u contents between 0.10 and 0.15. Plagioclase is also unzoned and classified as oligoclase (An_{27-30}).

The *P–T* isochemical phase diagram of the Grt-And-Crd-Bt schist sample 3A2 for temperatures between 400 and 725 °C and pressures within the 1.5 – 7.0 kbar range is shown in Fig. 7a. The Crd + And-rich nodules display an assemblage constituted by Crd + Qz + And + Pl + Bt + Grt + Ilm (Fig. 6b). Phengite and chlorite are interpreted as retrograde mineral phases partially replacing cordierite, andalusite and biotite. The observed mineral assemblage is reproduced in the model by the stability field Pl-Ilm-Grt-Bt-Crd-And-Qz (shaded in blue in Fig. 7a-c). Calculated compositional isopleths for XFe in cordierite within the peak assemblage field are between ~0.325 and 0.4 (Fig. 7b) in line with the observed compositions (0.35 and 0.40). Based on the pyrope isopleths (observed X_{Prp} = 0.12), *P–T* conditions of ~610 °C; 4 kbar, near the andalusite-sillimanite field boundary are found (Fig. 7b, c). Optimal *P–T* conditions of 589 +20/−30 °C and 3.8 +0.1/−1 kbar were obtained using Bingo-Antidote (Fig. 7d). The uncertainty envelope was calculated using a 2% threshold value on Q_{total}. At these conditions, the observed compositions of garnet and cordierite are modeled within their relative compositional uncertainties (see envelopes of model quality factors Q_{cmp} for each mineral in Fig. 7d) whereas biotite and plagioclase compositions are best modeled at slightly higher-pressure conditions (4–5 kbar). The *P–T* maps of model quality factors (Q_{asm}, Q_{vol}, Q_{cmp} and Q_{total}) are shown in Supplementary figure 2.

The *P–T* isochemical phase diagram of the Grt-St-Bt schist sample 10 is shown in Supplementary figure 1. The absence of aluminosilicate hampers a precise determination of the *P–T* conditions for this sample. However, assuming that in the Seridó Belt, staurolite occurs within the andalusite field, as suggested by Lima (1987, 1992), peak temperatures are between ~530 and 590 °C. In the *P–T* isochemical phase diagram calculated for the Grt-And-Sil-Crd-Bt schist sample 5, the *P–T* conditions of the Pl-Ilm-Grt-Bt-Crd-And-Qz stability field are 550–610 °C; 3–4 kbar. The late sillimanite overprint (Fig. 5e) indicates that higher temperature conditions were achieved at the metamorphic peak, but the absence of partial melting constrains maximum temperatures of ~670 °C (Supplementary figure 1).

6. Monazite petrochronology results

This section presents monazite data including textural context of monazite grains, internal structures, trace element patterns and U-Th-Pb geochronology. U-Th-Pb data are presented for samples 26B, 26A, 10, 5, 3A and 3A2 and trace element data for samples 26B and 3A. Weighted average dates are reported as X ± Y [Z] where Y is the 2 sigma-standard error and Z is the accuracy of 2% assumed for the LA-ICP-MS technique based on several long-term studies on reference materials materials (e.g. Košler et al., 2013; Kylander-Clark, 2017; Kylander-Clark et al., 2013; Spencer et al., 2013). Analytical procedures are described in Appendix A. U-Th-Pb monazite data are given in Supplementary data 2, trace element data in Supplementary data 3 and location of all analyzed spots in Supplementary data 4.

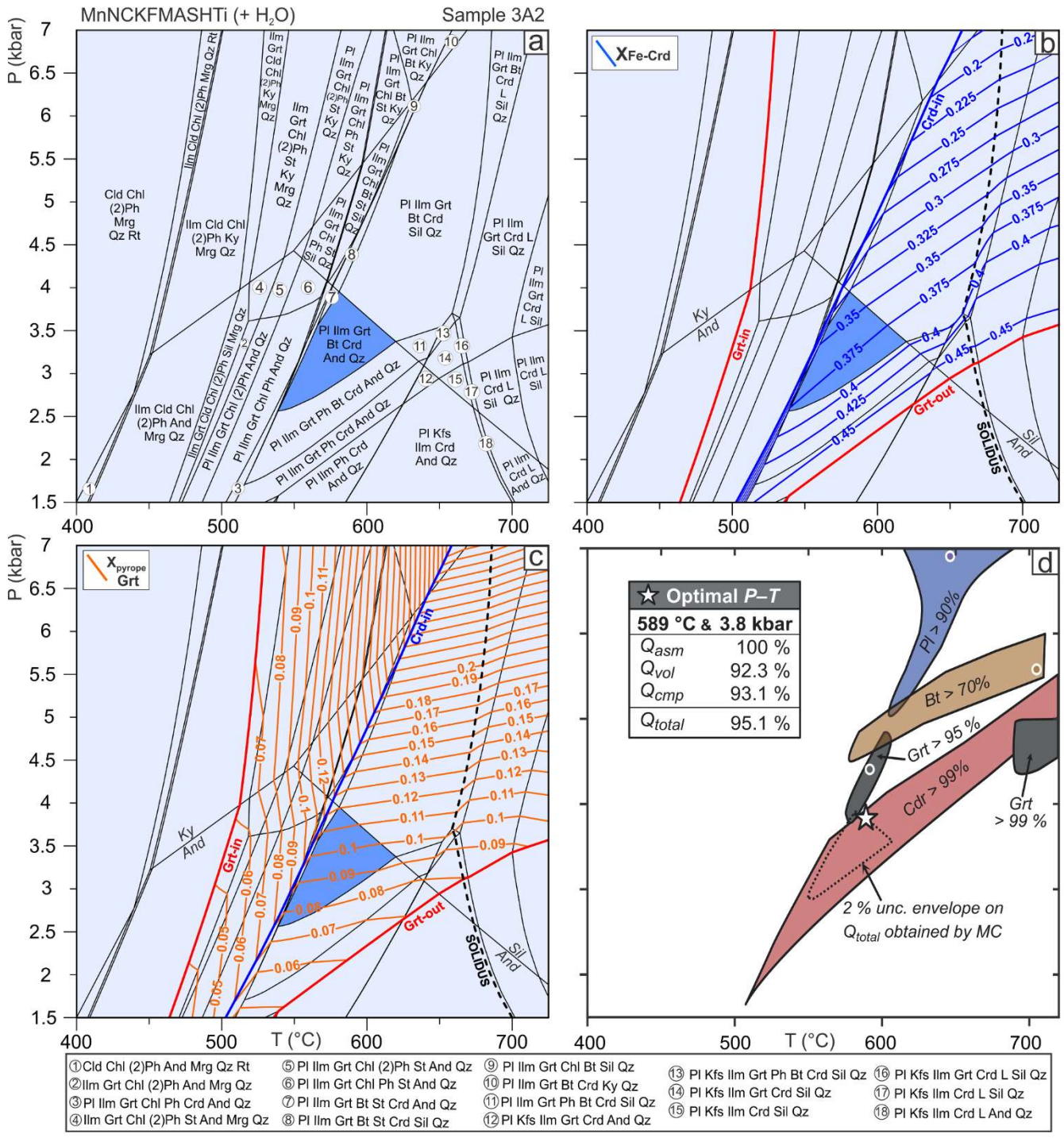

Fig. 7. (a) Calculated *P–T* isochemical phase diagram in the MnNCKFMASHTi system for the local composition of a cordierite + andalusite-rich nodule from sample 3A2 (see Fig. 6a, b); Isopleths are shown in (b) for X_{Fe} in cordierite (interval of 0.025) and (c) for X_{prp} in garnet (interval of 0.01). (d) Synthetic *P–T* diagram summarizing the results of Bingo-Antidote. The star shows the optimal solution obtained by inversion using recipe #1 of Antidote. The values of the model quality factors for the mineral assemblage (Q_{asm}), modes (Q_{vol}) and compositions (Q_{cmp}) as well as the global evaluation faction (Q_{total}) are given in percent (Lanari and Duesterhoeft, 2019; Duesterhoeft and Lanari, 2020). The dashed line shows the uncertainty envelope obtained using a Monte Carlo search function using a threshold value of 2% on Q_{total}. The colored areas show the optimal conditions derived for each solid solution based on the quality factors (Q_{cmp}); dots show the position of the local maxima in each domain.

6.1. Samples 26B and 26A

The leucosome-rich garnet-biotite metatexite sample 26B have monazite ranging from ~ 50 to 250 μm in size. Larger grains (150–250 μm) display well-developed core-rim textures, with sector-zoned BSE-bright cores wrapped by thick (50–100 μm) dark rims (Fig. 8c). Small grains usually do not show well-defined internal textures. The Th/U ratios of rims (6–19) are lower than cores (18–36), because the rims have lower Th (avg. 42235 ppm) and much higher U (avg. 5244 ppm) contents compared to the cores (avg. Th = 54805 ppm; avg. U = 1814 ppm). Rare earth elements (REE) data reduction was done using a fixed Ce value (23.05 wt%) as internal standard (see Appendix A) and

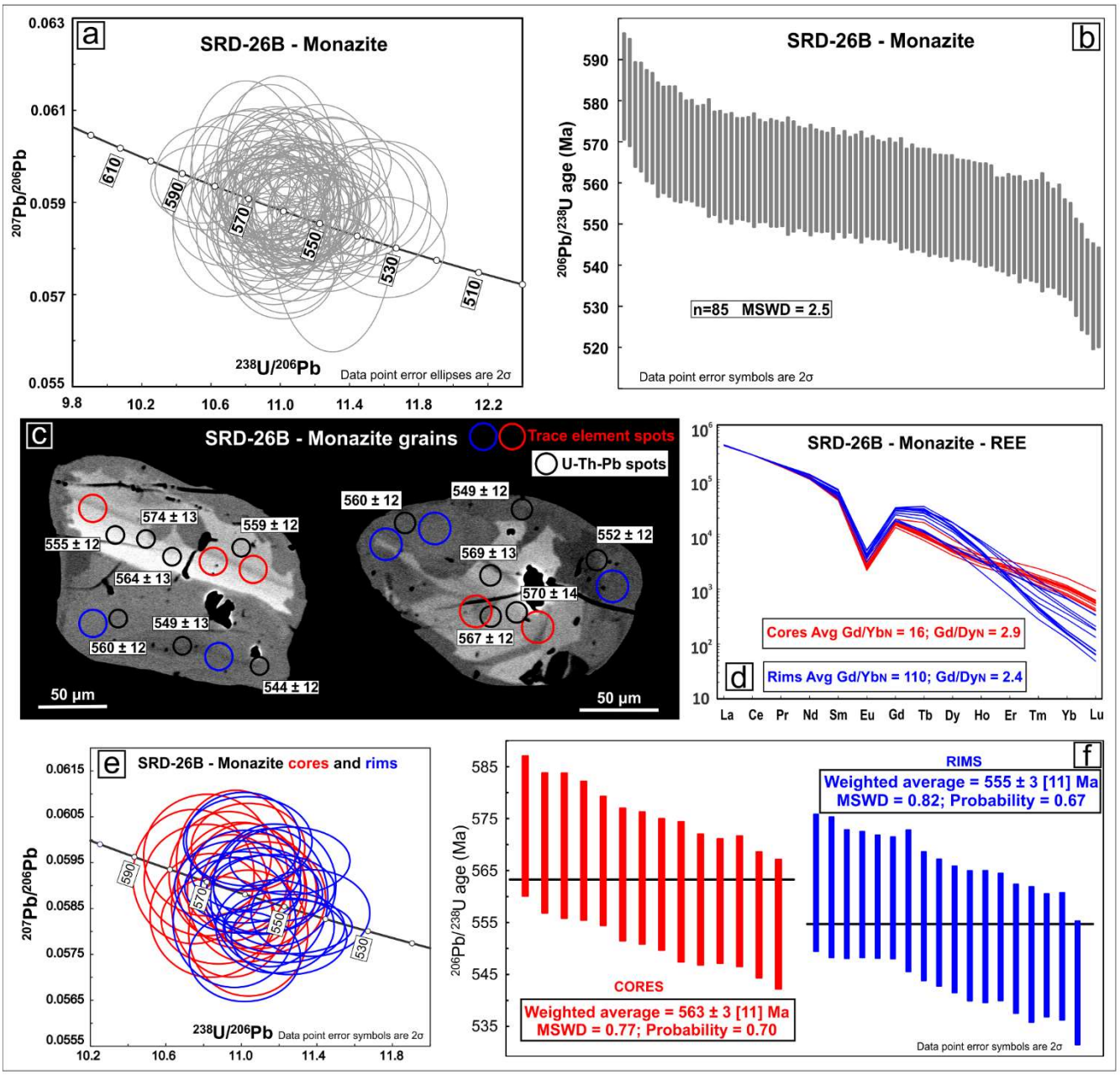

Fig. 8. Sample 26B monazite data. (a) Tera-Wasserburg U-Pb plot for all analyses from sample 26B; (b) Weighted average plot of the $^{206}Pb/^{238}U$ dates (n = 85; MSWD = 2.5); (c) Backscattered electron images (BSE) of representative monazite grains displaying well-defined core and rims textures. Black circles represent U-Th-Pb spots with $^{206}Pb/^{238}U$ dates reported next to each analysis. Red circles represent trace element spots on cores and blue circles spots on rims; (d) Chondrite-normalized (Boynton, 1984) REE patterns. Red symbols represent core analyses and blue symbols rims; (e) Tera-Wasserburg plot for U-Pb analyses on grains with well-defined core and rims textures. Red symbols represent core analyses and blue symbols rims; (f) Analyses on well-defined cores yield a weighted average $^{206}Pb/^{238}U$ date of 563 ± 3 [11] Ma (n = 14; MSWD = 0.77; Probability = 0.70). Analyses on well-defined rims yield a weighted average $^{206}Pb/^{238}U$ date of 555 ± 3 [11] Ma (n = 18; MSWD = 0.82; Probability = 0.67).

therefore absolute element contents cannot be compared between analyses. However, the shapes of the REE patterns and the element ratios can be used as petrogenetic indicators. Sample 26B monazite rims show highly fractionated heavy rare earth elements (HREE) patterns with average Gd/Yb_N of 110 compared to 16 in the cores. These rims are relatively enriched in Tb and Dy yielding average Gd/Dy_N of 2.4 compared to 2.9 in the cores (Fig. 8d) and also display slightly higher Y contents (avg. Y cores = 6323 ppm; avg. Y rims = 8646 ppm). The all eighty-five analyzed spots of sample 26B yield individual $^{206}Pb/^{238}U$ dates ranging from 580 ± 13 to 532 ± 12 Ma (MSWD = 2.5) (Fig. 8a, b). Th/Pb dates display a slightly larger spread ranging from 591 ± 14 to 521 ± 12 Ma (MSWD = 3.1) (Supplementary figure 3). The U-Th-Pb data spread is higher than can be explained by analytical uncertainties alone (Wendt and Carl, 1991). Analyses on large grains with well-developed core-rim textures (Fig. 8c) yield a weighted average $^{206}Pb/^{238}U$ age of 563 ± 3 [11] Ma (MSWD = 0.77; n = 14) for the cores and a weighted average $^{206}Pb/^{238}U$ age of 555 ± 3 [11] Ma (MSWD = 0.82; n = 18) for the rims (Fig. 8e, f).

Monazite grains from the garnet-biotite metatexite sample 26A are small, varying from 20 to 50 µm. Most grains do not display well-defined internal structures and the few grains that display core-rim textures in BSE images yielded dates that are indistinguishable (Fig. 9a). The Th/U ratios vary from 0.3 to 9.2 and do not correlate with dates. The majority of the monazite occurs as inclusions in biotite, but few small monazite

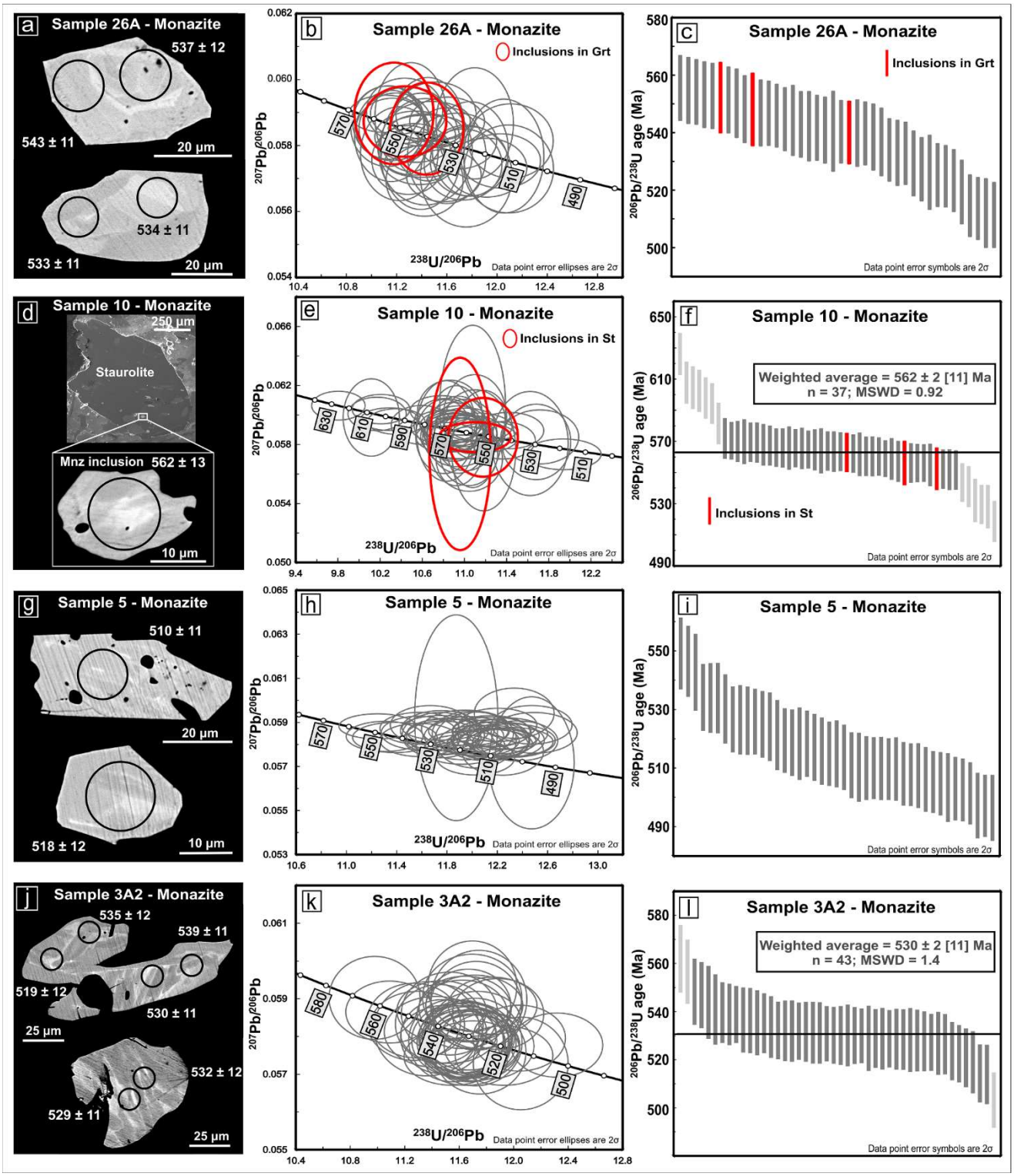

Fig. 9. (a-c) Sample 26A monazite data; (a) Backscattered electron images (BSE) of representative monazite grains with $^{206}Pb/^{238}U$ dates next to each spot; (b) Tera-Wasserburg U-Pb plot; (c) $^{206}Pb/^{238}U$ dates range between ca. 556 and 512 Ma. Red symbols represent monazite inclusion in garnet; (d-f) Sample 10 monazite data; (d) BSE images displaying monazite inclusion in staurolite outer rim; (e) Tera-Wasserburg U-Pb plot; (f) $^{206}Pb/^{238}U$ dates display large spread, but there is a well-defined cluster of dates between ca. 572 and 552 Ma that yield a weighted average date of 562 ± 2 [11] (n = 37; MSWD = 0.92). Red symbols represent monazite inclusions in staurolite; (g-i) Sample 5 monazite data; (g) BSE images of representative monazite grains; (h) Tera-Wasserburg U-Pb plot; (i) $^{206}Pb/^{238}U$ dates display large spread between ca. 549 and 496 Ma; (j-l) Sample 3A2 monazite data; (j) BSE images of representative monazite grains; (k) Tera-Wasserburg U-Pb plot; (l) Excluding three spots, the remaining 43 analyses yield a weighted average $^{206}Pb/^{238}U$ date of 530 ± 2 [11] Ma (MSWD = 1.4).

grains occur as inclusions in garnet inner rims. The obtained U-Pb dates show a large spread (MSWD = 5.1) with individual $^{206}Pb/^{238}U$ dates ranging from 556 ± 11 to 512 ± 11 Ma (n = 40) (Fig. 9b, c). The U-Pb dates from monazite inclusions in garnet are between 552 ± 12 and 540 ± 11 Ma (n = 3; Fig. 9b, c). Th/Pb dates display a similar spread varying between 561 ± 12 and 508 ± 11 Ma (MSWD = 4.8) (Supplementary figure 3).

6.2. Sample 10

The garnet-staurolite-biotite schist sample 10 display very small monazite grains from 15 to 40 μm in length. Most of the grains are inclusions in biotite and few are included in staurolite outer rims (Fig. 9d). The monazite grains do not show well-defined internal structure patterns in BSE images (Supplementary data 4). The Th/U ratios of the analyses vary from 3.8 to 30 and do not correlate with dates. The

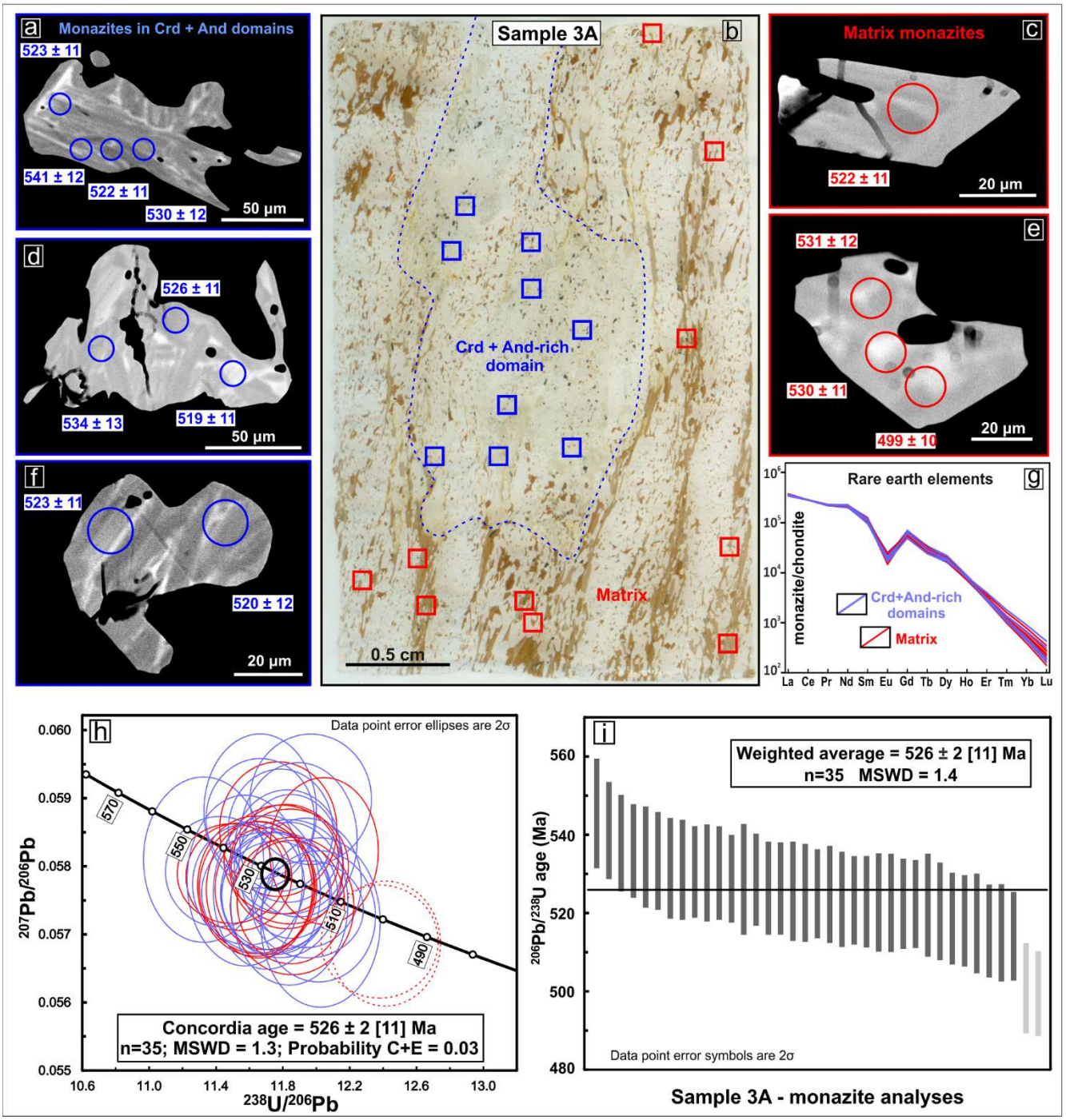

Fig. 10. Sample 3A monazite data. (a, d, f) Backscattered electron images (BSE) of monazite grains that occur within the andalusite + cordierite-rich domains with $^{206}Pb/^{238}U$ dates next to each spot; (b) Sample 3A thin section with location of monazite grains within the andalusite + cordierite-rich domains in blue and matrix monazite in red; (c, e) BSE images of matrix monazite grains; (g) Chondrite-normalized (Boynton, 1984) REE patterns of monazite grains from andalusite + cordierite-rich domains and matrix; (h) Tera-Wasserburg U-Pb plot. Excluding two matrix monazite outliers, the remaining matrix spots together with monazite from andalusite + cordierite-rich domains yield a concordia age of 526 ± 2 [11] Ma (n = 35; MSWD = 1.3); (i) Excluding two outliers, the remaining $^{206}Pb/^{238}U$ dates spread between ca. 545 and 514 Ma with a weighted average of 526 ± 2 [11] Ma (n = 35; MSWD = 1.4).

obtained U-Pb dates show a large spread with $^{206}Pb/^{238}U$ dates ranging from 626 ± 13 to 519 ± 12 Ma. Th/Pb dates display a very similar spread with $^{208}Pb/^{232}Th$ dates ranging from 628 ± 14 to 518 ± 13 Ma (Supplementary figure 3). However, there is a cluster of $^{206}Pb/^{238}U$ dates between 572 ± 12 and 552 ± 12 Ma that yields a weighted average date of 562 ± 2 [11] Ma (n = 37; MSWD = 0.92) (Fig. 9e, f). The monazite grains included in staurolite outer rims (Fig. 9d) yielded dates from 563 ± 12 to 552 ± 13 (n = 3; Fig. 9e, f), overlapping the weighted average date of ca. 562 Ma.

6.3. Sample 5

The garnet-andalusite-sillimanite-cordierite-biotite schist sample 5 has monazite grains ranging from ca. 20 to 50 μm in length. Most grains are inclusions in cordierite and biotite and do not show well-defined internal textures in BSE images (Fig. 9g) (Supplementary data 4). The Th/U ratios are mostly between 5 and 14 and do not correlate with dates. The obtained $^{206}Pb/^{238}U$ dates display a large spread, ranging from ca. 549 ± 12 to 496 ± 11 Ma (n = 43; MSWD = 5.5) (Fig. 9h, i). The Th/Pb data display a slightly larger spread with $^{208}Pb/^{232}Th$ dates ranging between 564 ± 12 and 496 ± 15 Ma (MSWD = 6.8) (Supplementary figure 3).

6.4. Samples 3A and 3A2

The garnet-andalusite-cordierite-biotite schist sample 3A2 is dominated by Crd + And-rich domains and display monazite grains ranging from ca. 50 to 150 μm in length with irregular shapes and complex internal textures (Fig. 9j) (Supplementary data 4). The Th/U ratios range from 6 to 17 and do not correlate with obtained dates. The obtained $^{206}Pb/^{238}U$ dates range from 562 ± 13 to 503 ± 11 (Fig. 9k, l) whereas $^{208}Pb/^{232}Th$ dates vary from 550 ± 13 to 500 ± 12 Ma (Supplementary figure 3). Excluding three outliers, the remaining forty-three analyses yield a weighted average $^{206}Pb/^{238}U$ date of 530 ± 2 [11] Ma (MSWD = 1.4) (Fig. 9k, l). Monazite grains from the garnet-andalusite-cordierite-biotite schist sample 3A occur in two distinct textural contexts (Fig. 10b). Small (ca. 20 – 50 μm long) subhedral to euhedral grains are inclusions in matrix biotite (Fig. 10c, e), whereas larger grains (up to 150 μm long), with very irregular shapes, occur within the Crd + And-rich domains, as inclusions in andalusite and cordierite (Fig. 10a, d, f). The larger grains have complex internal textures with thin (1–10 μm thick) BSE-bright stripes chaotically distributed within the grain's interior (Fig. 10a, d, f). Th/U ratios of matrix monazite vary from 3 to 16 and of monazite from Crd + And-rich domains from 5 to 11. The Th/U ratios do not correlate with obtained dates and the chondrite-normalized REE patterns of monazite from different textural contexts are similar (Fig. 10g). Monazite grains from both domains display highly fractionated HREE patterns with average Gd/Yb_N of 102 in matrix monazite and of 118 in monazite from Crd + And-rich domains. The Y contents of monazite grains from matrix and from the Crd + And-rich domains are also similar (avg. Y cores = 11424 ppm; avg. Y rims = 11288 ppm). The dates obtained from different textural domains are indistinguishable (Fig. 10h, i). The obtained $^{206}Pb/^{238}U$ dates range from 545 ± 14 to 499 ± 10 (Fig. 10h, i) whereas $^{208}Pb/^{232}Th$ dates display a larger spread varying from 563 ± 16 to 492 ± 10 Ma (Supplementary figure 3). Excluding two outliers, the remaining 35 U-Pb analyses yield a concordia age of 526 ± 2 [11] Ma (MSWD = 1.3) (Fig. 10h).

7. Discussion

7.1. Petrochronological constraints

7.1.1. Patos Shear Zone

Peak metamorphic conditions of the eastern Patos Shear Zone (Fig. 1b, c) were determined using conventional thermobarometry by Souza et al. (2006). The authors obtained temperatures between 670 and 765 °C and pressures ranging from 3.8 to 5.7 kbar (Fig. 11a), characterizing the low-pressure, high-temperature nature of the metamorphic event. The leucosome-rich garnet-biotite metatexite sample 26B displays large (150–250 μm) monazite grains with well-defined core-rim textures in BSE images (Fig. 8c). The rims display fractionated HREE patterns (Fig. 8d) that may be interpreted as a result of monazite growth in the presence of garnet, near peak *P–T* conditions. In this case, the weighted average $^{206}Pb/^{238}U$ date of 555 ± 3 [11] Ma (sample 26B; Fig. 8f) would be the best approximation of peak metamorphism age. Alternatively, the rims trace element signatures may be interpreted as a result of resorption of highly fractionated garnet rims with negative HREE slopes during the retrograde path. This hypothesis is corroborated by the Y enrichment in the rims. In this case, the rims age of ca. 555 Ma would represent a minimum age for the peak metamorphic conditions in the eastern Patos Shear Zone. BSE-bright and Th-rich monazite cores from this sample (26B) yield a weighted average date of 563 ± 3 [11] Ma (Fig. 8f.). Several studies have associated Th-rich monazite domains to the growth of monazite in the presence of melt (e.g. Dumond et al., 2015; McFarlane and Frost, 2009; Rocha et al., 2017). The age obtained for the Th-rich cores is within error the U-Pb dates obtained from migmatite zircon rims in the central portion of the Patos Shear Zone, ranging from ca. 573 to 562 Ma (Archanjo et al., 2013; Viegas et al., 2014), Therefore, the date of ca. 563 Ma obtained from the BSE-bright Th-rich monazite cores from sample 26B is interpreted as the best estimate of the age of the metamorphic peak under supersolidus conditions within the eastern Patos Shear Zone.

Monazite from biotite-rich migmatite domains within the eastern Patos Shear Zone display a large spread of $^{206}Pb/^{238}U$ dates, from ca. 556 to 512 Ma (sample 26A; Fig. 9b, c), that cannot be explained by analytical uncertainties alone. These dates most likely result from prolonged monazite growth within this time interval that could be related to protracted deformation and metamorphism within the shear zone. Slow cooling rates within the Patos Shear Zone are also constrained by amphibole ^{40}Ar-^{39}Ar ages between ca. 544 and 534 Ma and muscovite ^{40}Ar-^{39}Ar ages ranging from ca. 511 to 500 Ma (Monié et al., 1997; Corsini et al., 1998) (Fig. 11c).

7.1.2. Seridó Belt and Picuí Shear Zone

Metamorphic conditions of the Seridó Belt metasedimentary rocks have been previously determined in a campaign-style study using conventional thermobarometry by Lima (1987, 1992) (Fig. 11a). The author interprets high-geothermal gradients and an eastward increase of *P–T* conditions ranging from ca. 500–550 °C; 3 kbar in the western belt to ca. 600 °C; 4 kbar in the inner and eastern belt. A precise determination of *P–T* conditions of the sample in the western portion of the belt (sample 10) is precluded by the absence of aluminosilicate. However, considering the assumption of Lima (1987, 1992), that in the Seridó Belt staurolite occurs within the andalusite stability field, we can assume peak temperatures between ~530 and 590 °C at ~3–4 kbar (Supplementary figure 1). Monazite data from this sample show a large spread of $^{206}Pb/^{238}U$ dates ranging from ca. 626 to 519 Ma with a well-defined cluster between ca. 572 and 552 Ma, which yields a weighted average of 562 ± 2 [11] Ma (Fig. 9e, f). This cluster includes spots on monazite inclusions in staurolite outer rims (Fig. 9d). Assuming that important monazite growth is expected at the staurolite-in isograd (e.g. Kohn and Malloy, 2004), this is interpreted as the best staurolite age estimate. Therefore, it suggests that minimum temperatures of ~530 °C were achieved in the western belt at this time. The staurolite crystals display folded internal foliations (Fig. 5c) demonstrating that deformation was active at the timing of staurolite formation or was already active before, during prograde metamorphism. The younger group of dates from sample 10 largely deviates from the main population spreading from ca. 544 to 519 Ma and may be interpreted to result from monazite late (re) crystallization.

The rocks from the eastern (samples 3A and 3A2) and inner (sample

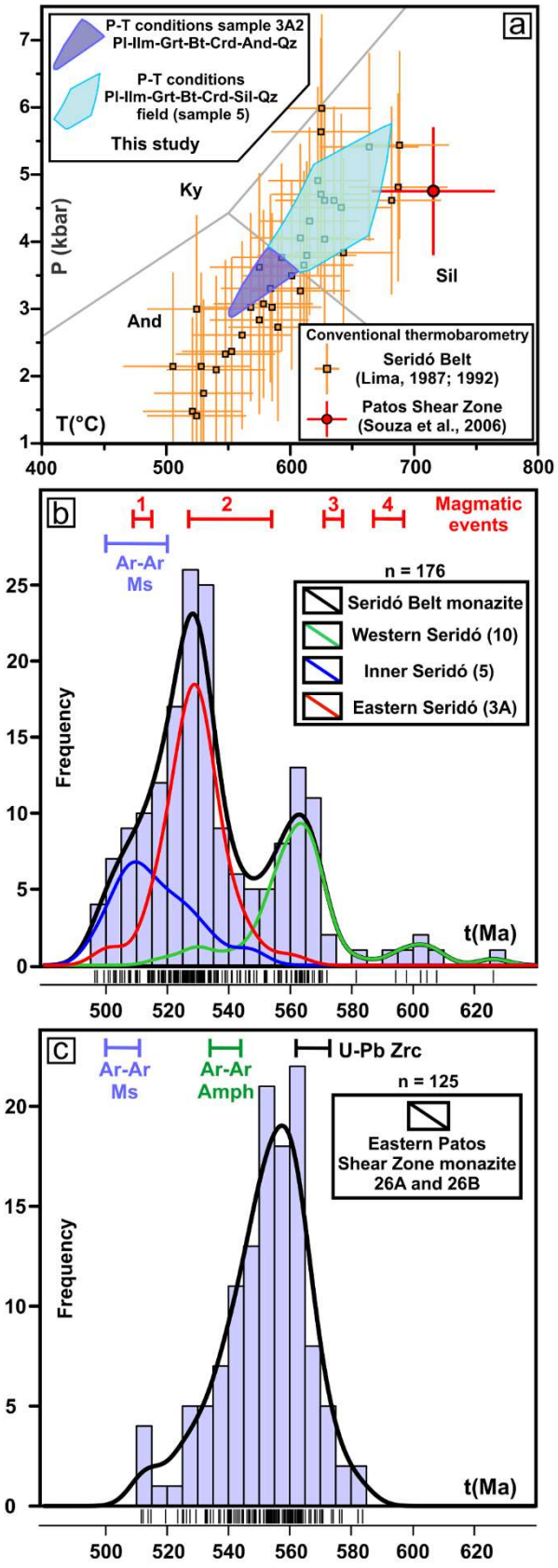

(caption on next column)

Fig. 11. (a) Comparison between *P-T* data from the literature (Lima, 1987, 1992; Souza et al., 2006) and results from this study; (b) Kernell density estimation (KDE) plot (5 Ma bandwith) of monazite data ($^{206}Pb/^{238}U$ dates) for samples within the Seridó Belt. Magmatic events: 1 – Pegmatitic granites; 2 – High-K calc-alkaline equigranular suite; 3 - High-K calc-alkaline porphyritic suite; 4 – Shoshonitic suite. Muscovite ^{40}Ar-^{39}Ar data from Araújo et al. (2005); (c) KDE plot (5 Ma bandwith) of monazite data ($^{206}Pb/^{238}U$ dates) for samples within the eastern Patos Shear Zone. U-Pb zircon data from Archanjo et al. (2013) and Viegas et al. (2014). Amphibole and muscovite ^{40}Ar-^{39}Ar data from Corsini et al. (1998). The KDE plots were produced with IsoplotR (Vermeesch, 2018).

5) Seridó Belt were metamorphosed within the cordierite + andalusite stability field. Observed mineral compositions associated with conventional and iterative thermodynamic models, both based on a local bulk composition of a Crd + And-rich nodule of sample 3A2, allowed peak metamorphic conditions of ~550–600 °C; 3–4 kbar to be retrieved (Figs. 7 and 11a). Sample 5 displays sillimanite overprinting the foliation (Fig. 5e) suggesting that slightly higher temperatures of ~600–670 °C (Supplementary figure 1) were reached in the inner portion of the Seridó Belt. In sample 3A, monazite inclusions in andalusite and cordierite have trace element patterns similar to matrix grains (Fig. 10g), indicating that both monazite populations are related to this low-pressure metamorphic stage (at ca. 590 °C and 3.8 kbar). These grains display individual $^{206}Pb/^{238}U$ dates ranging from ca. 545 to 514 Ma that yield a weighted average of 526 ± 2 [11] Ma (Fig. 10h, i), similar to the weighted average date obtained from sample 3A2 (531 ± 2 [11] Ma; Fig. 9l). These dates are interpreted as the maximum age of formation of cordierite + andalusite porphyroblasts in the eastern Seridó Belt. In these samples, eye-shaped Crd + And-rich nodules are elongated within the ~NNE-SSW Picuí Shear Zone (Fig. 2a) and are wrapped by the foliation (Fig. 4), indicating that deformation persisted after their generation. This demonstrates that deformation within the Picuí Shear Zone (Seridó Belt eastern boundary; Fig. 1c, 2a) lasted until at least ca. 530 – 525 Ma (i.e. maximum age of deformation). Monazite grains from the inner portion of the belt show a larger spread of dates between ca. 549–497 Ma (sample 5), which suggest protracted monazite growth within this age range that in great part overlaps the range of dates obtained from the eastern Seridó Belt samples (samples 3A and 3A2) (Fig. 11b).

7.2. *Tectonic evolution of a long-lived hot intracontinental orogeny*

The structural pattern of the Seridó Belt has been interpreted as a result of a general transpressive deformation controlled by displacement along the Patos Shear Zone, which squeezed the metasedimentary belt between more rigid basement domains (e.g. Corsini et al., 1991; Archanjo et al., 2002). The main planar structure in the belt is characterized by gently to moderately dipping foliations that delineate upright subhorizontal open to close folds with hinge lines parallel to the belt orientation (NNE-SSW) (Fig. 1c and 2a). These gently to moderately dipping foliations are transposed in the main shear zones (i.e. Patos and Picuí shear zones) by steep mylonitic foliations (Figs. 1c and 2). Some authors (e.g. Jardim de Sá, 1995) have correlated the gently to moderately dipping foliations to a Dn deformation phase and the steep foliations within the shear zones to a later Dn + 1 deformation phase. Recently, Domingos et al. (2020) have interpreted NNE-SSW striking magnetic and gravity anomalies within the Seridó Belt as migmatite-gneiss domes generated in association with the strike-slip shear zones. Assuming the existence of these domes underneath the metasedimentary sequence, the gently to moderately dipping foliations and the shear zones could be generated as a result of the same progressive deformation phase, being the local transposition within the shear zones a result of strain localization and partitioning. The similar spread of monazite dates of samples from regions of gently dipping foliations in the inner part of the belt (sample 5) and from the Picuí Shear Zone in the eastern belt

(samples 3A and 3A2) (Fig. 11b, c) is an argument in favor of simultaneous and long-lasting development of these distinct foliations in different parts of the Seridó Belt.

In summary, the results presented in this study together with data from the literature demonstrate that the intracontinental deformation in the Seridó Belt and associated Patos Shear Zone were long-lived, starting at ca. 580–575 Ma and enduring until at least ca. 530–525 Ma. Archanjo et al. (2002) have shown that plutons with ages of ca. 580–575 Ma display well-developed sub-horizontal NE-SW striking magnetic lineations attesting that deformation within the NE-SW striking shear zones were already active at this time. We cannot ascertain if that is a result of episodic or continuous deformation, but the presented data indicate that deformation was active before and after the staurolite formation at ca. 562 Ma in schists from the western Seridó Belt and persisted at least until ca. 530–525 Ma (i.e. maximum deformation age) in the eastern Seridó Belt within the NNE-SSW striking Picuí Shear Zone. Our data also suggest that deformation was associated with high-geothermal gradient conditions. Low-pressure migmatites from the Patos Shear Zone reached peak metamorphic conditions (~670–760 °C; 4–6 kbar) before ca. 553 Ma, most likely between ca. 573 and 563 Ma, indicating that anomalous geothermal conditions were effective at this time. Cordierite + andalusite-bearing schists from the inner and eastern Seridó Belt display individual monazite dates ranging mostly from ca. 550 to 500 Ma, with averages of ca. 530–515 Ma, demonstrating the long persistence of the high-geothermal gradient conditions in the region. Pegmatite intrusions are concentrated in the eastern and inner parts of the Seridó belt (Fig. 1c) and display ages ranging from ca. 515 to 509 Ma (e.g. Baumgartner et al., 2006). These ages partially overlap the dates obtained from the Crd + And-rich schists and are considerably younger than the main granitoid intrusions (Fig. 11b). Therefore, their generation cannot be linked to the evolution of the granitoid plutons and it is most likely related to low degrees of partial melting of the metasedimentary sequence driven by the high geothermal gradient conditions that persisted throughout the lower to middle Cambrian periods in the Seridó Belt.

The long-lived high geothermal conditions are also supported by ^{40}Ar-^{39}Ar data from the literature that indicate slow cooling (3–4 °C/Ma) of the Seridó Belt region between 580 and 500 Ma (e.g. Corsini et al., 1998). This demonstrates the existence of domains with different thermal evolution within the northern Borborema Province. The Ceará domain to the west of the Seridó Belt (Fig. 1b) displays much faster cooling rates (20–40 °C/Ma) (e.g. Ávila et al., 2020) and reached temperatures below 320 °C at ca. 560 Ma. This indicates that intracontinental deformation at the Ediacaran-Cambrian transition was concentrated in the inner portion of the Borborema Province far from the suture zones.

In comparison with other known intracontinental orogens, the Seridó Belt would share the long-term deformational history with the Musgrave Province (Smithies et al, 2011; Gorczyk et al., 2015; Walsh et al., 2015) and Alice Springs Orogeny (Shaw et al., 1991; Haines et al., 2001). However, the level of exposure in the Musgrave Province is much deeper than in the Seridó Belt, revealing UHT metamorphic conditions in lower to middle crustal levels (Wade et al., 2008; Walsh et al., 2015). Furthermore, the anomalous high geothermal gradient persisted for ~150 Myr in the Musgrave Orogeny (Walsh et al., 2015), which exceeds the time span of high geothermal gradient constrained in this study for the Seridó Belt. Differently from the Seridó Belt (see discussion below), delamination processes seem to explain the long-lasting anomalous geothermal gradient and voluminous bimodal magmatism of the Musgrave Province (Gorczyk and Vogt, 2015; Gorczyk et al., 2015). On the other hand, the long-lasting evolution of the Alice Springs Orogeny is broadly linked with episodic tectonic events occurring in the eastern margin of the Australian plate, recorded along the Tasman Orogenic System (Raimondo et al., 2014). Recent proposals of intracontinental evolution for other Ediacaran/Cambrian Pan-African/Brasiliano hot orogens include shear belt systems (the Ribeira, Dom Feliciano and Kaoko belts; Meira et al., 2019, 2020; Florisbal et al., 2012; De Toni et al., 2020; Konopásek et al., 2020) and a plateau-like confined orogen (the Araçuaí Orogen; Cavalcante et al., 2018, 2019; Fossen et al., 2020). These orogenic systems were also developed during several tens of millions of years (>70 Myr) and were controlled by strain localization and partitioning in weak continental lithosphere bounded by stiff cratonic domains (e.g. Cavalcante et al., 2018; Meira et al., 2019).

The diversity of tectonic processes recorded in these different orogens reinforce the importance of intracontinental deformation and orogeny in shaping Earth's surface, especially in those orogens related to the West Gondwana assembly and supercontinent cycles (e.g., Aitken et al., 2013; Meira et al., 2015, 2020). Although intracontinental orogeny is still underappreciated by the Precambrian geological community, detailed petrochronological studies in natural laboratories, like the Borborema Shear Zone System, must provide insights into the evolution of this first-order component of global tectonics.

7.3. The geodynamic significance of the low-pressure assemblages

Low-pressure orogenic belts characterized by the occurrence of andalusite/sillimanite as stable aluminosilicates in metapelites, abundant granitoid intrusions and slow to very slow exhumation rates (e.g. Myashiro, 1961; Zwart, 1967; De Yoreo et al., 1991; Vilà et al., 2007) are common features in different geodynamic scenarios, including magmatic arcs, extensional environments and collisional settings (e.g. De Yoreo et al., 1991). In all cases, the close relationship between low-pressure metamorphic rocks and granitoid intrusions invariably raises the major question: are the plutons heat sources or only a result of heating that caused regional metamorphism? (e.g. Thompson, 1989; De Yoreo et al., 1991; Peixoto et al., 2018; Dziawa et al., 2019).

In the Seridó Belt, the occurrence of widespread low-pressure (high *T/P*) assemblages has long been recognized (e.g. Lima, 1992; Mello and Mello, 1974), but their geodynamic significance has not yet been explored in detail. Some authors have argued that these low-pressure assemblages are the result of contact metamorphism related to the Neoproterozoic granitoid intrusions (e.g. Chagas et al., 2018; Souza et al., 2007). Although the plutonic activity could have contributed to the heat transport through the crust by advection, the Seridó Belt metasedimentary rocks show evidence that the low-pressure metamorphism was regional and long-lived instead of local and episodic. Campaign-style studies have shown that the low-pressure assemblages are widespread within the belt and are not restricted to pluton aureoles (Lima, 1987, 1992; Mello and Mello, 1974) (Fig. 11a). These studies have also shown a relatively constant high-geothermal gradient throughout the belt that would not be expected if the metamorphism were driven by localized heat sources. Moreover, the low-pressure minerals (i.e. andalusite and cordierite) are oriented along the foliation (Fig. 5d, f). These minerals display internal foliations parallel to the matrix foliation indicating they were not rotated after formation and are therefore syntectonic (Fig. 5f). The absence of prograde chemical zoning in garnet porphyroblasts from the Crd + And-bearing sample 3A2 (Fig. 6c-f) may also be an evidence that the low-pressure metamorphic event was long-lived allowing enough time for the prograde garnet zoning to be erased by diffusion (e.g. Kohn, 2013). Additionally, it is important to mention the strong coupling between plutons and host rocks magnetic fabrics (Archanjo et al., 2002), which suggest slow cooling of intrusions under high-temperature conditions.

High-geothermal gradient conditions associated with regional low-pressure (high *T/P* ratios) metamorphism can be attained in collisional settings by crustal thickening (England and Thompson, 1984; De Yoreo et al., 1991). Models considering crustal thickening and the influence of heat-producing elements (HPE) generate clockwise metamorphic *P–T* paths, which achieve low-pressure conditions, within the andalusite stability field, during the retrograde evolution (e.g. England and Thompson, 1984). These models are unlikely to explain the Seridó Belt metamorphic evolution as the andalusite-bearing assemblages are

prograde, testified by late sillimanite overprinting (Fig. 5e). Moreover, in these models, low-pressure metamorphism is post-deformational what is clearly not the case of the Seridó Belt, where low-pressure assemblages are interpreted as syntectonic. Delamination of the lower crust and lithospheric mantle driven by intracontinental compression would generate long-lived anomalous high-geothermal gradients and complex deformational patterns due to asthenosphere upwelling and pervasive melting of crust and mantle (e.g. Gorczyk and Vogt, 2015; Gorczyk et al., 2015). However, delamination processes would promote fast uplift (e.g. Kay and Kay, 1993) which is opposed to the slow cooling rates and therefore slow exhumation rates determined for the Seridó Belt region (Corsini et al., 1998; Araújo et al., 2005).

Thompson (1989) has proposed a model that is able to explain the occurrence of regional *syn*-deformational low-pressure metamorphism and associated magmatism. In this model, a previously tectonically thinned sialic crust and overlying basins are homogeneously shortened and thickened soon after extension (<10 Myr). As the pre-shortening geotherms were already steep, crustal rocks could reach low-pressure conditions in a prograde sense and *syn*-deformationally. It also explains the generation of crustal melts during deformation and the slow uplift rates as the final crustal thickness do not exceed much the normal values. Provenance studies (Van Schmus et al., 2003; Hollanda et al., 2015) have suggested that the Seridó Group metasedimentary sequences were deposited during the late Neoproterozoic, between 650 and 610 Ma, most likely in an extensional setting. Therefore, extension took place just before compressional deformation what makes the model of Thompson (1989) a plausible model to explain the Seridó Belt tectonic evolution. Alternative models for the generation of high-geothermal conditions include those proposed by Neves and Mariano (2004) and Neves et al. (2008) where an enrichment of heat-producing elements (HPE) in the subcontinental mantle lithosphere would be responsible for the decrease of lithospheric strength and therefore strain localization, added by local increase in the geothermal gradients. Another possible mechanism for the generation of the high geothermal gradient conditions could be channelized astenospheric upwelling toward this region induced by development of the thick lithospheric keels of the adjoining blocks. Regardless of the mechanisms that have led to high-geothermal gradient conditions, these conditions were crucial to reduce the continental lithosphere strength and allow widespread intracontinental deformation and associated magmatism. Therefore, the long-lived anomalous thermal structure is most likely the reason behind and not a result of the Borborema Shear Zone System.

8. Conclusions

The data provided in this contribution lead us to the following conclusions:

- The Borborema Province intracontinental deformation was long-lived starting before ca. 580 Ma and lasting until at least ca. 530–525 Ma (i.e. maximum deformation age).
- In the Seridó Belt region, the deformation was associated to high-geothermal gradients that led to widespread low-pressure (high *T*/*P* ratios) metamorphism.
- Metasedimentary rocks from the eastern portion of the belt record peak metamorphic conditions of ca. 550−600° C; 3 – 4 kbar, within the andalusite + cordierite stability field, while rocks from the inner portion reached slightly higher temperatures within the sillimanite + cordierite stability field.
- The long-lived anomalous thermal conditions were responsible to reduce the lithosphere strength allowing extensive intracontinental deformation and associated magmatism.
- Igneous intrusions could have played an important role to advect heat through the lithosphere, but they are most likely a result of the regional thermal anomaly and not the cause of it.
- Regardless the mechanism that generated the long-lived regional high-geothermal gradient conditions, they were essential for the reworking of the Borborema Province continental interior, allowing the formation and maintenance of the Borborema Shear Zone System.

CRediT authorship contribution statement

Caue R. Cioffi: Conceptualization, Investigation, Formal analysis, Visualization, Writing - original draft. **Vinícius T. Meira:** Conceptualization, Investigation, Visualization, Writing - review & editing. **Ricardo I. F. Trindade:** Conceptualization, Funding acquisition, Writing - review & editing. **Pierre Lanari:** Investigation, Formal analysis, Writing - review & editing. **Carlos E. Ganade:** Investigation, Writing - review & editing. **Axel Gerdes:** Investigation, Formal analysis, Writing - review & editing.

Declaration of Competing Interest

The authors declare that they have no known competing financial interests or personal relationships that could have appeared to influence the work reported in this paper.

Acknowledgements

This research was supported by São Paulo Research Foundation (FAPESP)/CAPES grant #2016/25987-0 to C.R.C; FAPESP grants #2018/07892-8 to C.R.C and #2016/06114-6 to R.I.F.T; Conselho Nacional de Desenvolvimento Científico e Tecnológico (CNPq) grant #404767/2016-8 to V.T.M and Serrapilheira Institute grant #Serra - 1709-21887 to C.E.G. This is FIERCE contribution No. 58. Linda Marko and Richard Albert are acknowledged for their help with LA-ICP-MS analyses at GUF. Constructive reviews by Catherine Mottram, Sérgio P. Neves and an anonymous reviewer helped us to improve the manuscript and are appreciated. Wilson Teixeira and Elson Paiva are thanked for editorial handling.

Appendix A. – Analytical methods

Monazite U-Th-Pb and trace element data were obtained by LA-ICP-MS using a Resolution S-155 (Resonetics) 193nm ArF excimer laser ablation system coupled to a ThermoScientific Element XR sector field ICP-MS at the FIERCE, Goethe-University Frankfurt (GUF). Prior to the analyses, the internal structures of the grains were investigated with backscattered electron images (BSE) obtained using a JEOL JSM-6490 scanning electron microscope (SEM) at the Department of Geosciences of the GUF. Monazite samples were analyzed *in-situ* on thin sections allowing the preservation of the grain's textural context. Monazite U-Th-Pb LA-ICP-MS analyses were performed with high-spatial resolution using 13μm circular laser spots what was needed as several of the analyzed grains are small (ca. 20-30 μm long). Data has been acquired during 3 individual sessions. Unknowns were bracketed with the GJ-1 zircon standard (Jackson et al., 2004) to correct for U/Pb fractionation, $^{207}Pb/^{206}Pb$ mass bias and drift correction over the duration of the sequence. A correction factor to account for the difference in $^{206}Pb/^{238}U$ fractionation between monazite and zircon has been determined prior to the analyses using Nama monazite in-house reference (Wolfgang Dörr, Uni. Frankfurt, personal communication; ID-TIMS $^{206}Pb/^{238}U$ age of 1027 ± 1 Ma). This offset of about 3.5% on the $^{206}Pb/^{238}U$ fractionation between zircon and monazite is due to the different behavior during laser ablation and plasma ionization and the different spot size used (13 μm vs 30 μm). $^{206}Pb/^{238}U$ error is the quadratic additions of the within run precision (2 SE) and the external reproducibility (2 SD) of the primary reference material (GJ-1 zircon). $^{207}Pb/^{206}Pb$ error propagation (^{207}Pb signal dependent) following Gerdes & Zeh (2009). $^{207}Pb/^{235}U$ error is the quadratic addition of $^{207}Pb/^{206}Pb$ and $^{206}Pb/^{238}U$

uncertainties. Monazite Bananeira, Manangotry and Nama were analyzed as secondary standards during the analytical sessions to verify accuracy and repeatability of the applied method. U-Th-Pb data reduction was done with an in-house excel spreadsheet (Gerdes and Zeh, 2006, 2009). Bananeira monazite (Gonçalves et al., 2016; $^{207}Pb/^{235}U$ ID-TIMS age = 507.7 ± 1.3 Ma) yielded a weighted average $^{206}Pb/^{238}U$ age of 508.3 ± 2.8 Ma (n = 24, MSWD = 1.5), Nama monazite a weighted average $^{206}Pb/^{238}U$ age of 1029.7 ± 4.2 Ma (n = 26; MSWD = 1.05) and Manangoutry monazite (Paquette and Tiepolo, 2007; upper intercept ID-TIMS age = 555 ± 2 Ma) a weighted average $^{206}Pb/^{238}U$ age of 552.7 ± 3.1 Ma (n = 20; MSWD = 0.27). Based on repeated analyses of those reference monazites during 2017–2019, the long-term reproducibility of the method at GUF is about 1 to 1.5%. Weighted average and concordia plots were produced with Isoplot (Ludwig, 2003). Monazite trace element analyses were performed after the U-Pb analyses on large monazite grains from samples 26B and 3A. Monazite trace element analyses were performed with 20 µm circular spots and the reference material NIST612 was used as a primary standard. Trace element data reduction was done with the IOLITE 2.5 software package (Paton et al., 2011) using a fixed Ce value (23.05 wt%) as internal standard.

The nodular garnet-andalusite-cordierite-biotite schist sample 3A2 was selected for major mineral chemical analyses. Selected thin sections were analyzed by electron probe micro-analyzer (EPMA) at the Institute of Geological Sciences of the University of Bern using both quantitative spot analyses and X-ray compositional mapping in wavelength-dispersive mode. Compositional maps were generated according to the procedures described in Lanari et al. (2012) and Lanari et al. (2013) with 15kV accelerating voltage, 100 nA beam and dwell times of 120 ms. Compositional maps were converted into oxide weight percentage maps using XMapTools (Lanari et al., 2014, 2019).

Appendix B. Supplementary data

Supplementary data to this article can be found online at https://doi.org/10.1016/j.precamres.2021.106141.

References

Abdelsalam, M.G., Liégeois, J.-P., Stern, R.J., 2002. The Saharan Metacraton. J. Afr. Earth Sc. 34, 119–136.

Aitken, A.R.A., 2011. Did the growth of Tibetan topography control the locus and evolution of Tien Shan mountain building? Geology 39, 459–462.

Aitken, A.R.A., Raimondo, T., Capitanio, F.A., 2013. The intraplate character of supercontinent tectonics. Gondwana Res. 24, 807–814.

Almeida, F.F.M., Hasui, Y., Brito Neves, B.B., Fuck, R.A., 1981. Brazilian structural provinces: An introduction. Earth-Sci. Rev. 17, 1–29.

Araújo, M.N.C., Silva, F.C.A., Jardim de Sá, E.F., 2001. Pegmatite emplacement in the Seridó Belt, northeastern Brazil: Late stage kinematics of the Brasiliano Orogen. Gondwana Res. 4, 75–85.

Araújo, M.N.C., Silva, F.C.A., Jardim de Sá, E.F., Holcombe, R.J., Vasconcelos, P.M., 2003. Microstructural evolution of the Seridó Belt, Ne-Brazil: The effect of two tectonic events on development of c-axis preferred orientation in quartz. J. Struct. Geol. 25, 2089–2107.

Araújo, M.N.C., Vasconcelos, P.M., Silva, F.C.A., Jardim de Sá, E.F., Sá, J.M., 2005. 40Ar/39Ar geochronology of gold mineralization in Brasiliano strike-slip shear zones in the Borborema Province, NE Brazil. J. S. Am. Earth Sci. 19, 445–460.

Archanjo, C.J., Trindade, R.I.F., Bouchez, J.L., Ernesto, M., 2002. Granite fabrics and regional-scale strain partitioning in the Seridó belt (Borborema Province, NE Brazil). Tectonics 21 (1).

Archanjo, C.J., Viegas, L.G.F., Hollanda, M.H.B.M., Souza, L.C., Liu, D., 2013. Timing of the HT/LP transpression in the Neoproterozoic Seridó Belt (Borborema Province, Brazil): Constraints from U-Pb (SHRIMP) geochronology and implications for the connections between NE Brazil and West Africa. Gondwana Res. 23, 701–714.

Ávila, C.F., Archanjo, C.J., Hollanda, M.H.B.M., Macêdo Filho, A.A., Lemos-Santos, D.V., 2020. Shear zone cooling and fabrics of synkinematic plutons evidence timing and rates of orogenic exhumation in the northwest Borborema Province (NE Brazil). Precambr. Res. 350.

Avouac, J.P., Tapponnier, P., 1993. Kinematic model of active deformation in Central Asia. Geophys. Res. Lett. 20, 895–898.

Baldwin, J.A., Powell, R., Brown, M., Moraes, R., Fuck, R.A., 2005. Modelling of mineral equilibria in ultrahigh-temperature metamorphic rocks from the Anápolis-Itauçu Complex, central Brazil. J. Metamorph. Geol. 23, 511–531.

Baumgartner, R., Romer, R.L., Moritz, R., Sallet, R., Chiaradia, M., 2006. Columbite-tantalite granitic pegmatites from the Seridó Belt, northeastern Brazil: genetic constraints from U-Pb dating and Pb isotopes. Can. Mineral. 44, 69–86.

Bezerra, F.H.R., Amaral, R. F., Silva, F.O., Sousa, M.O.L., Legrand, J.M., Sá, J.M., Maia, H.N., Fonseca, V.P., Vieira, M.M., Souza, L.C., 2009. Nota explicativa da folha Jardim do Seridó 1:100.000 (SB.25-Z-B-V). CPRM, Brasil.

Boynton, W.V., 1984. Cosmochemistry of the rare earth elements: meteorite studies. In: Henderson, P. (Ed.), Developments in geochemistry. Elsevier, pp. 63–114.

Brito Neves, B.B., Santos, E.J., Van Schmus, R., 2000. Tectonic history of the Borborema Province. In: Cordani, U.G., Milani, E.J., Thomaz Filho, A., Campos, D.A. (Eds), Tectonic Evolution of South America, 31° International Geological Congress, Rio de Janeiro, pp. 151-182.

Bueno, J.F., Oliveira, E.P., McNaughton, N.J., Laux, J.H., 2009. U-Pb dating of granites in the Neoproterozoic Sergipano Belt, NE-Brazil: Implications for the timing and duration of continental collision and extrusion tectonics in the Borborema Province. Gondwana Res. 15, 86–97.

Burov, E.B., 2011. Rheology and strength of the lithosphere. Mar. Pet. Geol. 28 (8), 1402–1443.

Burov, E.B., Watts, A.B., 2006. The long-term strength of continental lithosphere: "jelly sandwich" or "crème brûlée"? GSA Today 16, 4–10.

Caby, R., Arthaud, M.H., Archanjo, A.J., 1995. Lithostratigraphy and petrostructural characterization of supracrustal units in the Brasiliano Belt of northeast Brazil: geodynamic implications. J. S. Am. Earth Sci. 8, 235–246.

Cavalcante, R., Cunha, A.L.C., Oliveira, R.G., Medeiros, V.C., Dantas, A.R., Costa, A.P., Cavalcanti, C.A., Larizzatti, J.H., 2016. Metalogenia das Províncias Minerais do Brasil: Área Seridó-Leste, extremo nordeste da Província Borborema (RN-PB): escala 1:250.000.

Cavalcante, R., Cunha, A.L.C., Costa, A.P., Dantas, A.R. 2018. Carta geológica-geofísica: folha Picuí 1:100.000 (SB.24-Z-B-VI). CPRM, Brasil.

Cavalcante, C., Hollanda, M.H.B.M., Vauchez, A., Kawata, M., 2018. How long can the middle crust remain partially molten during orogeny? Geology 46, 839–842.

Cavalcante, C., Fossen, H., de Almeida, R.P., Hollanda, M.H.B.M., Egydio-Silva, M., 2019. Reviewing the puzzling intracontinental termination of the Araçuaí-West Congo orogenic belt and its implications for orogenic development. Precambr. Res. 322, 85–98.

Caxito, F.A., Santos, L.C.M.L., Ganade, C.E., Bendaoud, A., Fettous, E., Bouyo, M.H., 2020. Toward an integrated model of geological Evolution for the NE Brazil-NW Africa: The Borborema Province and its connections to the Trans-Saharan (Benino-Nigerian and Tuareg shields) and Central Africa orogens. Braz. J. Geol. 50, 1–38.

Chagas, C.F., Souza, Z.S., Moreira, J.A.M., 2018. Auréola termal provocada pela intrusão do pluton Totoró em micaxistos do Grupo Seridó, Ediacarano da Província Borborema, Ne do Brasil. Geologia USP, Série Científica 18, 117–139.

Coggon, R., Holland, T.J.B., 2002. Mixing properties of phengitic micas and revised garnet-phengite thermobarometers. J. Metamorph. Geol. 20, 683–696.

Corsini, M., Vauchez, A., Archanjo, C., Jardim de Sá, E.F., 1991. Strain transfer at continental scale from a transcurrent sear zone to a transpressional fold belt: The Patos-Seridó system, northeastern Brazil. Geology 19, 586–589.

Corsini, M., Figueiredo, L.L., Caby, R., Féraud, G., Ruffet, G., Vauchez, A., 1998. Thermal history of the Pan-African/Brasiliano Borborema Province of northeast Brazil deduced from 40Ar/39Ar analysis. Tectonophysics 285, 103–117.

Cunningham, D., 2005. Active intracontinental transpressional mountain building in the Mongolian Altai: defining a new class of orogen. Earth Planet. Sci. Lett. 240, 436–444.

Cunningham, D., 2013. Mountain building processes in intracontinental oblique deformation belts: Lessons from the Gobi Corridor, Central Asia. J. Struct. Geol. 46, 255–282.

Dantas, E.L., Van Schmus, W.R., Hackspacker, P.C., Fetter, A.H., Brito Neves, B.B., Cordani, U., Nutman, A.P., Williams, I.S., 2004. The 3.4-3.5 Ga São José do Campestre Massif, NE Brazil: remnants of the oldest crust in South America. Precambr. Res. 130, 113–137.

Dantas, E.L., Souza, Z.S., Wernick, E., Hackspacker, P.C., Martin, H., Xiaodong, D., Li, J.-W., 2013. Crustal growth in the 3.4-2.7 Ga São José de Campestre Massif, Borborema Province NE Brazil. Precambr. Res. 227, 120–156.

De Andrade, V., Vidal, O., Lewin, E., O'Brien, P., Agard, P., 2006. Quantification of electron microprobe compositional maps of rock thin sections: an optimized method and examples. J. Metamorph. Geol. 24, 655–668.

De Toni, G.B., Bitencourt, M.F., Nardi, L.V.S., Florisbal, L.M., Almeida, B.S., Geraldes, M., 2020. Dom Feliciano Belt orogenic cycle tracked by its pre-collisional magmatism: The Tonian (ca. 800 Ma) Porto Belo Complex and its correlations in southern Brazil and Uruguay. Precambr. Res. 342.

De Yoreo, J.J., Lux, D.R., Guidotti, C.V., 1991. Thermal modelling in low-pressure/high-temperature metamorphic belts. Tectonophysics 188, 209–238.

de Capitani, C., Brown, T.H., 1987. The computation of chemical equilibrium in complex systems containing non-ideal solutions. Geochim. Cosmochim. Acta 51, 2639–2652.

de Capitani, C., Petrakakis, K., 2010. The computation of equilibrium assemblage diagrams with Theriak/Domino software. Am. Mineral. 95, 1006–1016.

Domingos, N.R.R., Medeiros, W.E., Oliveira, R.G., 2020. Geophysical evidence for doming during the Pan-African/Brasiliano orogeny in the Seridó belt, Borborema Province, Brazil. Precambr. Res. 350.

Duesterhoeft, E., Lanari, P., 2020. Iterative thermodynamic modelling – Part 1: A theoretical scoring technique and a computer program (Bingo-Antidote). J. Metamorph. Geol. 38, 1–25.

Dumond, G., Gonçalves, P., Williams, M.L., Jercinovic, M.J., 2015. Monazite as a monitor of melting, garnet growth and feldspar recrystallization in continental lower crust. J. Metamorph. Geol. 33, 735–762.

Dziawa, C., Gaidies, F., Percival, J., 2019. Conditions and timing of low-pressure – high-temperature metamorphism in the Montresor Belt, Rae Province, Nunavut. Can. J. Earth Sci. 56, 654–671.
England, P.C., Thompson, A.B., 1984. Pressure-temperature-time paths of regional metamorphism I. Heat transfer during the evolution of regions of thickened continental crust. J. Petrol. 894–928.
Fetter, A.H., Santos, T.J.S., Van Schmus, R., Hackspacker, P., Brito Neves, B.B., Arthaud, M.H., Nogueira Neto, J.A., Wernick, E., 2003. Evidence for Neoproterozoic continental arc Magmatism in the Santa Quitéria Batholith of Ceará State, NW Borborema Province, NE Brazil: Implications for the assembly of West Gondwana. Gondwana Res. 6, 265–273.
Florisbal, L.M., Janasi, V.A., Bitencourt, M.F., Heaman, L.M., 2012. Space–time relation of post-collisional granitic magmatism in Santa Catarina, southern Brazil: U-Pb LA-MC-ICP-MS zircon geochronology of coeval mafic-felsic magmatism related to the Major Gercino Shear Zone. Precambr. Res. 216, 132–151.
Fossen, H., Cavalcante, C., Konopásek, J., Meira, V.T., Almeida, R.P., Hollanda, M.H.B. M., Trompette, R., 2020. A critical discussion of the subduction-collision model for the Neoproterozoic Araçuaí-West Congo orogen. Precambr. Res. 343, 1–10.
Ganade de Araujo, C.E., Cordani, U.G., Basei, M.A.S., Castro, N.A., Sato, K., Sproesser, W. M., 2012. U-Pb detrital zircon provenance of metasedimentary rocks from the Ceará Central and Médio Coreaú domains, Borborema Province, NE-Brazil: Tectonic implications for a long-lived Neoproterozoic active continental margin. Precambr. Res. 206–207, 36–51.
Ganade de Araujo, C.E., Weinberg, R.F., Cordani, U.G., 2014a. Extruding the Borborema Province (NE-Brazil): a two-stage Neoproterozoic collision process. Terra Nova 26, 157–168.
Ganade de Araujo, C.E., Rubatto, D., Hermann, J., Cordani, U.G., Caby, R., Basei, M.A.S., 2014b. Ediacaran 2,500-km-long synchronous deep continental subduction in the West Gondwana Orogen. Nat. Commun. 5.
Ganade, C.E., Cordani, U., Agbossoumounde, Y., Caby, R., Basei, M.A.S., Weinberg, R., Sato, K., 2016. Tightening-up NE Brazil and NW Africa connections: New U-Pb/Lu-Hf zircon data of a complete plate tectonic cycle in the Dahomey belt of the West Gondwana Orogen in Togo and benin. Precambr. Res. 276, 24–42.
Ganade, C.E., Basei, M.A.S., Granjean, F.C., Armstrong, R., Brito, R.S., 2017. Contrasting Archean (2.85-2.68 Ga) TTGs from the Tróia Massif (NE-Brazil) and their geodynamic implications for flat to steep subduction transition. Precambr. Res. 297, 1–18.
Gerdes, A., Zeh, A., 2006. Combined U-Pb and Hf isotope LA-(MC)-ICP-MS analyses of detrital zircons: Comparison with SHRIMP and new constraints for the provenance and age of an Armoican metasediment in Central Germany. Earth Planet. Sci. Lett. 249, 47–61.
Gerdes, A., Zeh, A., 2009. Zircon formation versus zircon alteration – New insights from combined U-Pb and Lu-Hf in-situ LA-ICP-MS analyses, and consequences for the interpretation of Archean zircon from the Central Zone of the Limpopo Belt. Chem. Geol. 261, 230–243.
Gonçalves, G.O., Lana, C., Scholz, R., Buick, I.S., Gerdes, A., Kamo, S.L., Corfu, F., Marinho, M.M., Chaves, A.O., Valeriano, C., Nalini Jr., H.A., 2016. As assessment of monazite from the Itambé pegmatite district for use as U-Pb isotope reference material for microanalysis and implications for the origin of the "Moacyr" monazite. Chem. Geol. 424, 30–50.
Gorczyk, W., Hobbs, B., Gessner, K., Gerya, T., 2013. Intracratonic geodynamics. Gondwana Res. 24, 838–848.
Gorczyk, W., Vogt, K., 2015. Tectonics and melting in intra-continental settings. Gondwana Res. 27, 196–208.
Gorczyk, W., Smithies, H., Korhonen, F., Howard, H., De Gromard, R.Q., 2015. Ultra-hot Mesoproterozoic evolution of intracontinental central Australia. Geosci. Front. 6, 23–37.
Gray, D.R., Foster, D.A., Meert, J.G., Goscombe, B.D., Armstrong, R., Trouw, R.A.J., Passchier, C.W., 2008. A Damara orogen perspective on the assembly of southwestern Gondwana. Geol. Soc. Lond. Special Publ. 294, 257–278.
Guimarães, I.P., Bittar, S.M.B., Silva, J.M.R., Silva, F.M.J., Araújo, D.B., Arruda, S.D.D., Alcantara, V.C., 2007. Nota explicativa da folha Solânea 1:100.000 (SB.25-Y-A-IV). CPRM, Brasil.
Guimarães, I.P., Van Schmus, W.R., Brito Neves, B.B., Bittar, S.M.B., Silva Filho, A.F., Armstrong, R., 2012. U-Pb zircon ages of orthogneisses and supracrustal rocks of the Cariris Velhos belt: Onset of Neoproterozoic rifting in the Borborema Province, NE Brazil. Precambr. Res. 192–195, 52–77.
Haines, P.W., Hand, M., Sandiford, M., 2001. Palaeozoic synorogenic sedimentation in central and northern Australia; a review of distribution and timing with implications for the evolution of intracontinental orogens. Aust. J. Earth Sci. 48, 911–928.
Holland, T.J.B., Powell, R., 1998. An internally consistent thermodynamic dataset for phases of petrological interest. J. Metamorph. Geol. 16, 309–343.
Holland, T.J.B., Baker, J.M., Powell, R., 1998. Mixing properties and activity-composition relationships of chlorites in the system MgO-FeO-Al2O3-SiO2-H2O. Eur. J. Mineral. 19, 395–406.
Hollanda, M.H.B.M., Archanjo, C.J., Souza, L.C., Liu, D., Armstrong, R., 2011. Long-lived Paleoproterozoic granitic magmatism in the Seridó-Jaguaribe domain, Borborema Province-NE Brazil. J. S. Am. Earth Sci. 32, 287–300.
Hollanda, M.H.B.M., Archanjo, C.J., Bautista, J.R., Souza, L.C., 2015. Detrital zircon ages and Nd isotope compostions of the Seridó and Lavras da Mangabeira basins (Borborema Province, NE Brazil): Evidence for exhumation and recycling associated with a major shift in sedimentary provenance. Precambr. Res. 258, 186–207.
Hollanda, M.H.B.M., Souza Neto, J.A., Archanjo, C.J., Stein, H., Maia, A.C.S., 2017. Age of the granitic magmatism and the W-Mo mineralization in skarns of the Seridó belt (NE Brazil) based on zircon U-Pb (SHRIMP) and molybdenite Re-Os dating. J. S. Am. Earth Sci. 79, 1–11.
Jackson, S.E., Pearson, N.J., Griffin, W.L., Belousova, E.A., 2004. The application of laser ablation-inductively coupled plasma spectrometry to in situ U-Pb geochronology. Chem. Geol. 47–69.
Jardim de Sá., E.F. 1994. A Faixa Seridó (Província Borborema NE do Brasil) e o seu significado geodinâmico na Cadeia Brasiliana/Pan-Africana. Brasília. Unpublished PhD Thesis, IG-UNB.
Jardim de Sá., E.F., Fuck, R.A., Macedo, M.H.F., Peucat, J.J., Kawashita, K., Souza, Z.S., Bertrand, J.M. 1995. Pre-Brasiliano orogenic evolution in the Seridó Belt, NE Brazil: Conflicting geochronological and structural data. Revista Brasileira de Geociências 25, 307–314.
Jordan, T.H., 1975. The comtinental tectosphere. Rev. Geophys. Space Phys. 13, 1–12.
Kay, R.W., Kay, M., 1993. Delamination and delamination magmatism. Tectonophysics 219, 177–189.
Kohn, M.J., 2013. Geochemical zoning in metamorphic minerals. Treat. Geochem. Second Ed. 4, 249–280.
Kohn, M.J., Malloy, M., 2004. Formation of monazite via prograde metamorphic reactions among common silicates: Implications for age determinations. Geochim. Cosmochim. Acta 68, 101–113.
Konopásek, J., Cavalcante, G.C.G., Fossen, H., Janoušek, V., 2020. Adamastor – An ocean that never existed? Earth Sci. Rev. https://doi.org/10.1016/j.earscirev.2020.103201.
Kylander-Clark, A.R.C., Hacker, B.R., Cottle, J.M., 2013. Laser-ablation split-stream ICP petrochronology. Chem. Geol. 345, 99–112.
Košler, J., Sláma, J., Belousova, E., Corfu, F., Gehrels, G.E., Gerdes, A., Horstwood, M.S. A., Sircombe, K.N., Sylvester, P.J., Tiepolo, M., Whitehouse, M.J., Woodhead, J.D., 2013. U-Pb detrital zircon analysis – Results of an inter-laboratory comparison. Geostandards Anal. Res. 37, 243–259.
Kylander-Clark, A.R.C., 2017. Petrochronology by Laser-Ablation inductively coupled plasma mass spectrometry. Rev. Mineral. Geochem. 83, 183–196.
Lanari, P., Guillot, S., Schwartz, S., Vidal, O., Tricart, P., Riel, N., Beyssac, O., 2012. Diachronous evolution of the alpine continental subduction wedge: evidence from P-T estimates in the Briançonnais Zone houillere (France – Western Alps). J. Geodyn. 56–57, 39–54.
Lanari, P., Riel, N., Guillot, S., Vidal, O., Schwartz, S., Pêcher, A., Hattori, K.H., 2013. Deciphering high-pressure metamorphism in collisional context using microprobe mapping methods: application to the Stak eclogiticmassif (northwest Himalaya). Geology 41 (2), 111–114.
Lanari, P., Vidal, O., de Andrade, V., Dubacq, B., Lewin, E., Grosch, E., Schawartz, S., 2014. XMAPTOOLS: A MATLAB-based program for electron microprobe X-ray image processing and geothermobarometry. Comput. Geosci. 62, 227–240.
Lanari, P., Engi, M., 2017. Local bulk composition effects on mineral assemblages. Rev. Mineral. Geochem. 83, 55–102.
Lanari, P., Duesterhoeft, E., 2019. Modeling metamorphic rocks using equilibrium thermodynamics and internally consistent databases: Past achievements, problems and perspectives. J. Petrol. 60, 19–56.
Lanari, P., Vho, A., Bovay, T., Airaghi, L., Centrella, S., 2019. Quantitative compositional mapping of mineral phases by electron probe micro-analyzer. Geol. Soc. Lond. Special Publ. 478, 39–63.
Lanari, P., Hermann, J., 2020. Iterative thermodynamic modelling—Part 2: tracing equilibrium relationships between minerals in metamorphic rocks. J. Metamorph. Geol. https://doi.org/10.1111/jmg.12575.
Liégeois, J.-P., Abdelsalam, M.G., Ennih, N., Ouabadi, A., 2013. Metacraton: Nature, genesis and behavior. Gondwana Res. 23, 220–237.
Lima, E.S., 1987. Evolução termo-barométrica das rochas metapelíticas da região do Seridó, nordeste brasileiro. Verista Brasileira Geociências 17, 315–323.
Lima, E.S., 1992. Metamorphic conditions in the Seridó region of northeastern Brazil during the Brasiliano Cycle (Late Proterozoic). J. S. Am. Earth Sci. 5, 265–273.
Long, L.E., Ketcham, D.H., Fanning, C.M., Sial, A.N., 2019. The unregenerated São Rafael pluton, Borborema Province, Northeast Brazil. Lithos 332–333, 192–206.
Ludwig, K.R., 2003. User's Manual for Isoplot 3.00, a Geochronological Toolkit for Microsoft Excel. Berkeley Geochronology Center Special Publication 4.
McFarlane, C.R.M., Frost, B.R., 2009. Constraints on the early metamorphic evolution of Broken Hill, Australia, from in-situ U-Pb dating and REE geochemistry of monazite. J. Metamorph. Geol. 27, 3–17.
Meira, V.T., Garcia-Casco, A., Juliani, C., Almeida, R.P., Schorscher, J.H.D., 2015. The role of intracontinental deformation in supercontinent assembly: Insights from the Ribeira Belt, southeastern Brazil (Neoproterozoic West Gondwana). Terra Nova 27, 206–217.
Meira, V.T., Garcia-Casco, A., Hyppolito, T., Juliani, C., Schorscher, J.H.D., 2019. Tectono-metamorphic Evolution of the Central Ribeira Belt, Brazi: A case of late Neoproterozoic intracontinental orogeny and flow of partially molten deep crust during the assembly of West Gondwana. Tectonics 38, 3182–3209.
Meira, V.T., Garcia-Casco, A., Hyppolito, T., Juliani, C., Schorscher, J.H.D., 2020. Reply to comment by Heilbonr and Valeriano on "Tectono-metamorphic Evolution of the Central Ribeira Belt, Brazi: A case of late Neoproterozoic intracontinental orogeny and flow of partially molten deep crust during the assembly of West Gondwana". Tectonics 39. https://doi.org/10.1029/2020TC006307.
Mello, A.A., Mello, Z.F., 1974. Metamorphic zoning in the Seridó region, northeastern Brazil. Revista Brasileira Geociências 4, 1–14.
Michaut, C., Jaupart, C., Mareschal, J.-C., 2009. Thermal evolution of cratonic roots. Lithos 109, 47–60.
Molnar, P., Tapponnier, P., 1975. Cenozoic tectonics of Asia: effects of a continental collision. Science 189, 419–426.
Monié, P., Caby, R., Arthaud, M.H., 1997. The Neoproterozoic Brasiliano orogeny in northeast Brazil: 40Ar/39Ar and petrostructural data from Ceará. Precambr. Res. 81, 241–264.

Myashiro, A., 1961. Evolution of metamorphic belts. J. Petrol. 2, 277–311.
Nascimento, M.A.L., Galindo, A.C., Medeiros, V.C., 2015. Ediacaran to Cambrian magmatic suites in the Rio Grande do Norte domain, extreme northeastern Borborema Province (NE of Brazil): Current knowledge. J. S. Am. Earth Sci. 58, 281–289.
Neves, S.P., Vauchez, A., Feraud, G., 2000. Tectono-thermal Evolution, magma emplacement, and shear zone development in the Caruaru area (Borborema Province, NE Brazil). Precambr. Res. 99, 1–32.
Neves, S.P., 2003. Proterozoic history of the Borborema province (NE Brazil): Correlations with neighboring cratons and Pan-African belts and implications for the evolution of western Gondwana. Tectonics 22, 1031.
Neves, S.P., Mariano, G., 2004. Heat-producing elements-enriched continental mantle lithosphere and Proterozoic intracontinental orogens: Insights from Brasiliano/Pan-African belts. Gondwana Res. 7, 427–436.
Neves, S.P., Tommasi, A., Vauchez, A., Hassani, R., 2008. Intraplate continental deformation: Influence of a heat-producing layer in the lithospheric mantle. Earth Planet. Sci. Lett. 274, 392–400.
Neves, S.P., 2015. Constraints from zircon geochronology on the tectonic evolution of the Borborema Province (NE Brazil): Widespread intracontinental reworking of a Paleoproterozoic accretionary orogen. J. S. Am. Earth Sci. 58, 150–164.
Neves, S.P., Silva, J.M.R., Bruguier, O., 2017. Geometry, kinematics and geochronology of the Sertânia Complex (central Borborema Province, NE Brazil): Assessing the role of accretionary versus intraplate processes during West Gondwana assembly. Precambr. Res. 298, 552–571.
Oliveira, E.P., Windley, B.F., Araújo, M.N.C., 2010. The Neoproterozoic Sergipano orogenic belt, NE Brazil: A complete plate tectonic cycle in western Gondwana. Precambr. Res. 181, 64–84.
Padilha, A.L., Vitorello, I., Pádua, M.B., Fuck, R.A., 2016. Deep magnetotelluric signatures of the early Neoproterozoic Cariris Velhos tectonic event within the Transversal sub-province of the Borborema Province, NE Brazil. Precambr. Res. 275, 70–83.
Paquette, J.L., Tiepolo, M., 2007. High resolution (5 μm) U-Th-Pb isotope dating of monazite with excimer laser ablation (ELA)-ICPMS. Chem. Geol. 240, 222–237.
Paton, C., Hellstrom, J., Paul, B., Woodhead, J., Hergt, J. 2011. Iolite: Freeware for the visualization and processing of mass spectrometry data. Journal of Analytical Atomic Spectrometry 26, 2508–2518. Geostandards and Geoanalytical Research 21 (1), 115–144.
Peixoto, E., Alkmim, F.F., Pedrosa-Soares, A., Lana, C., Chaves, A.O., 2018. Metamorphic record of collision and collapse in the Ediacaran-Cambrian Araçuaí orogen, SE-Brazil: Insights from P-T pseudosections and monazite dating. J. Metamorph. Geol. 36, 147–172.
Pereira, F.S., Rosa, M.L.S., Conceição, H., Bertotti, A.L., 2020. Age, composition, and source of the Macureré Mafic Suite, Southern Borborema Province, Brazil. Brazilian J. Geol. 50.
Raimondo, T., Collins, A.S., Hand, M., Walker-Hallam, A., Smithies, R.H., Evins, P.M., Howard, H.M., 2010. The anatomy of a deep intracontinental orogen. Tectonics 29 (4), TC4024.
Raimondo, T., Hand, M., Collins, W.J., 2014. Compressional intracontinental orogens: Ancient and modern perspectives. Earth Sci. Rev. 130, 128–153.
Rocha, B.C., Moraes, R., Möller, A., Cioffi, C.R., Jercinovic, M.J., 2017. Timing of anatexis and melt crystallization in the Socorro-Guaxupé Nappe, SE Brazil: Insights from trace element composition of zircon, monazite and garnet coupled to U-Pb geochronology. Lithos 277, 337–355.
Rodrigues, S.W.O., Medeiros, V.C. 2015. Geologia e recursos minerais da folha Campina Grande (1:100.000) (SB.25-Y-C-I).
Santos, E.J.S., Van Schmus, W.R., Kozuch, M., Brito Neves, B.B., 2010. The Cariris Velhos tectonic event in Northeast Brazil. J. S. Am. Earth Sci. 29, 61–76.
Santos, L.C.M.L., Dantas, E.L., Santos, E.J., Santos, R.V., Lima, H.M., 2015. Early to Late Paleoproterozoic magmatism in NE Brazil: The Alto Moxotó Terrane and its tectonic implications for the Pre-West Gondwana assembly. J. S. Am. Earth Sci. 58, 188–209.
Santos, L.C.M.L., Dantas, E.L., Cawood, P., Lages, G.A., Lima, H.M., Santos, E.J., 2018. Accretion tectonics in western Gondwana deduced from Sm-Nd isotope mapping of terranes in the Borborema Province, NE Brazil. Tectonics 37, 2727–2743.
Santos, T.J.S., Garcia, M.G.M., Amaral, W.S., Caby, R., Wernick, E., Arthaud, M.H., Dantas, E.L., Santosh, M., 2009. Relics of eclogites facies assemblages in the Ceará Central Domain, NW Borborema Province, NE Brazil: Implications for the assembly of West Gondwana. Gondwana Res. 15, 454–470.
Santos, T.J.S., Amaral, W.S., Ancelmi, M.F., Pitarello, M.Z., Fuck, R.A., Dantas, E.L., 2015. U-Pb age of the coesite-bearing eclogite from NW Borborema Province, NE Brazil: Implications for western Gondwana assembly. Gondwana Res. 28, 1183–1196.
Shaw, R.D., Etheridge, M.A., Lambeck, K., 1991. Development of the Late Proterozoic to Mid-Paleozoic, Intracratonic Amadeus Basin in central Australia: A key to understanding tectonic forces in plate interiors. Tectonics 10, 688–721.
Smithies, R.H., Howard, H.M., Evins, P.M., Kirkland, C.L., Kelsey, D.E., Hand, M., Wingate, M.T.D., Collins, A.S., Belousova, E., 2011. High-temperature granite magmatism, crust–mantle interaction and the Mesoproterozoic intracontinental evolution of the Musgrave Province, Central Australia. J. Petrol. 52, 931–958.
Souza, L.C., Legrand, J.M., Verkaeren, J., 2007. Metamorfismo térmico nos micaxistos Seridó em torno do batólito granítico de Acarí (RN), nordeste do Brasil: Química mineral de ilmenitas e turmalinas. Estudos Geológicos 17, 71–84.
Souza, Z.S., Montel, J.-M., Gioia, S.M.L.C., Hollanda, M.H.B.M., Nascimento, M.A.L., Jardim de Sá, E.F., Amaro Pimentel, V.E.M.M., Lardeaux, J.-M., Veschambre, M., 2006. Electron microprobe dating of monazite from high-T shear zones in the São José de Campestre Massif, NE Brazil. Gondwana Res. 9, 441–455.
Souza, Z.S., Martin, H., Peucat, J.-J., Jardim de Sá, E.F., Macedo, M.H.F., 2007. Calc-alkaline magmatism at the Archean-Proterozoic transition: the Caicó Complex basement (NE Brazil). J. Petrol. 48, 2149–2185.
Souza, Z.S., Kalsbeek, F., Deng, X.-D., Frei, R., Kokfelt, T.F., Dantas, E.L., Li, J.-W., Pimentel, M.M., Galindo, A.C., 2016. Generation of continental crust in the northern part of the Borborema Province, northeastern Brazil, from Archean to Neoproterozoic. J. S. Am. Earth Sci. 68, 68–96.
Spencer, K.J., Hacker, B.R., Kylander-Clark, A.R.C., Andersen, T.B., Cottle, J.M., Stearns, M.A., Poletti, J.E., Seward, G.G.E., 2013. Campaign-style titanite U-Pb dating by laser-ablation ICP: Implication for crustal flow, phase transformations and titanite closure. Chem. Geol. 341, 84–101.
Thompson, P.H., 1989. Moderate overthickening of thinned sialic crust and the origin of granitic magmatism and regional metamorphism in low-P-high-T terranes. Geology 17, 520–523.
Van Schmus, W.R., Brito Neves, B.B., Hackspacker, P.C., Babinski, M., 1995. U/Pb and Sm/Nd geochronologic studies of the eastern Borborema Province, northeastern Brazil: initial conclusions. J. S. Am. Earth Sci. 8, 267–288.
Van Schmus, W.R., Brito Neves, B.B., Williams, I.S., Hackspacker, P.C., Fetter, A.H., Dantas, E.L., Babinski, M., 2003. The Seridó Group of NE Brazil, a late Neoproterozoic pre- to syn-collisional basin in West Gondwana: Insights from SHRIMP U-Pb detrital zircon ages an SM-Nd crustal residence (TDM) ages. Precambr. Res. 127, 287–327.
Van Schmus, W.R., Kozuch, M., Brito Neves, B.B., 2011. Precambrian history of the Zona Transversal of the Borborema Province, NE Brazil: Insights from Sm-Nd and U-Pb geochronology. J. S. Am. Earth Sci. 31, 227–252.
Vauchez, A., Egydio-Silva, M., 1992. Termination of a continental-scale strike-slip fault partially melted crust: The West Pernambuco shear zone, northeast Brazil. Geology 20, 1007–1010.
Vauchez, A., Neves, S., Caby, R., Corsini, M., Egydio-Silva, M., Arthaud, M., Amaro, V., 1995. The Borborema shear zone system, NE Brazil. J. S. Am. Earth Sci. 8, 247–266.
Vermeesch, 2018. IsoplotR: A free and open toolbox for geochronology. Geosci. Front. 9, 1479–1493.
Viegas, L.G.F., Archanjo, C.J., Vauchez, A., 2013. Fabrics of migmatites and the relationships between partial melting and deformation in high-grade transpressional shear zones: The Espinho Branco anatexite (Borborema Province, NE Brazil). J. Struct. Geol. 48, 45–56.
Viegas, L.G.F., Archanjo, C.J., Hollanda, M.H.B.M., Vauchez, A., 2014. Microfabrics and zircon U-Pb (SHRIMP) chronology of mylonites from the Patos shear zone (Borborema Province, NE Brazil). Precambr. Res. 243, 1–17.
Vilà, M., Pin, C., Liesa, M., Enrique, P., 2007. LPHT metamorphism in a late orogenic transpressional setting, Albera Massif, NE Iberia: Implications for the geodynamic evolution of the Variscan Pyrenees. J. Metamorph. Geol. 25, 3221–3347.
Wade, B.P., Kelsey, D.E., Hand, M., Barovich, K.M., 2008. The Musgrave Province: stitching north, west and south Australia. Precambr. Res. 166, 370–386.
Walsh, A.K., Kelsey, D.E., Kirkland, C.L., Hand, M., Smithies, R.H., Clark, C., Howard, H. M., 2015. P-T-t evolution of a large, long-lived, ultrahigh-temperature Grenvillian belt in central Australia. Gondwana Res. 28, 531–564.
White, R.W., Powell, R., Holland, T.J.B., Worley, B.A., 2000. The effect of TiO2 and Fe2O3 on metapelitic assemblages at greenschist and amphibolite facies conditions: mineral equilibria calculations in the system K2O-FeO-MgO-Al2O3-SiO2-H2O-TiO2-Fe2O3. J. Metamorph. Geol. 15, 223–238.
White, R.W., Pomroy, N.E., Powell, R., 2005. An in situ metatexite-diatexite transition in upper amphibolite facies rocks from Broken Hill, Australia. J. Metamorph. Geol. 23, 579–602.
White, R.W., Powell, R., Holland, T.J.B., 2007. Progress relating to calculation of partial melting equilibria for metapelites. J. Metamorph. Geol. 25, 511–527.
Whitney, D.L., Evans, B.W., 2010. Abbreviations for names of rock-forming minerals. Am. Mineral. 95, 185–187.
Zwart, H.J., 1967. The duality of orogenic belts. Geol. Mijnbouw 46, 283–309.